Development of a 96-well Platform for the Bulk Production of Three-Dimensional Human Skeletal Muscle Microtissues

by

Haben Yemane Abraha

A thesis submitted in conformity with the requirements
for the degree of Master of Applied Science, Biomedical Engineering

Institute of Biomaterials & Biomedical Engineering
University of Toronto

96-well Platform for the Bulk Production of Three-Dimensional Human Skeletal Muscle Microtissues

Haben Yemane Abraha

Master of Applied Science, Biomedical Engineering

Institute of Biomaterials & Biomedical Engineering

University of Toronto

2018

Abstract

Skeletal muscle wasting is a largely untreatable condition wherein patients lose skeletal muscle strength, stamina, and protein content. We posit that the lack of skeletal muscle wasting treatments is due to the failings of existing skeletal muscle models. To address this problem, we developed a human muscle microtissue (hMMT) platform for bulk generation of reproducible, contractile, 3D hMMTs. hMMTs recapitulated key aspects of native human skeletal muscle, including muscle-specific protein expression, drug response, and contractility. Furthermore, the hMMT platform can non-invasively assess strength, and is exceedingly simple to fabricate. To illustrate hMMT platform utility, hMMTs were used with tumour-conditioned media to model cancer-associated muscle wasting *in vitro*. hMMTs were also used to screen chemotherapeutics, revealing that the drug irinotecan is toxic to human myofibers. Collectively, these results underline the considerable potential of the hMMT platform as a vehicle for skeletal muscle research and drug candidate validation.

Acknowledgments

Firstly, I would like to thank my supervisor Dr. Penney Gilbert for her guidance and support throughout the entirety of my Master's degree. Her insights regarding my project and the incredibly positive lab environment she has cultivated have been invaluable. In addition, I want to acknowledge my committee members Drs. Alison McGuigan and Jane Batt for their key advice regarding the focus and scope of my project. I would also like to thank all of the members of the Gilbert Lab for making my stay an enjoyable one. Special thanks to Mohsen Afshar and Sadegh Davoudi for their contributions to this work, and to Mohammad Afshar, whose work was integral to the success of this project. Finally, I wish to thank my parents, whom I will always owe my successes to, my brother Fidel, and Holly.

Table of Contents

List of Tables

List of Figures

List of Abbreviations

- **PDMS** – polydimethylsiloxane

- **hMMT** – human muscle microtissue

- **DMEM** – Dulbecco's modified eagle medium

- **FACS** – fluorescence-activated cell sorting

- **TCM** – tumour-conditioned media

- **IGF1** – insulin-like growth factor-1

- **MTT** – 3-[4,5-dimethylthiazol-2-yl]-2,5-diphenyl tetrazolium bromide salt

- **EdU** – 5-ethynyl-2'-deoxyuridine

- **HMGCoA reductase** – 3-hydroxy-3-methyl-glutaryl-coenzyme A reductase

Chapter 1: Introduction

1.1 – Skeletal muscle wasting

Skeletal muscle is present throughout the human body and comprises all voluntarily contractile muscle. The skeletal muscle is involved in a litany of bodily activities across multiple body systems, including but not limited to locomotion, swallowing, limb movement, blinking, and breathing[1]. As a result of this extensive integration throughout the human body, many pathological conditions which primarily target other systems have the additional effect of inducing skeletal muscle atrophy. Skeletal muscle atrophy, or skeletal muscle wasting, refers to an impairment of the skeletal muscle wherein the protein content, size, stamina, and force production of the skeletal muscle are dramatically reduced, while mortality is increased[2]. Skeletal muscle wasting-associated conditions run the etiological gamut, from chronic metabolic disorders such as type 2 diabetes mellitus (T2DM)[3,4], to all cancers[5], to Charcot-Marie Tooth (CMT) disease, a hereditary neurological disorder[6]. The manifestation of skeletal muscle wasting in these cases is itself clinically significant – skeletal muscle wasting is associated with a reduced quality of life, long-term functional disability, and decreased patient survival[7]. The clinical severity of skeletal muscle wasting is compounded by its pervasiveness. CMT is the most common heritable peripheral nervous system disorder, based on a 1 in 1214 prevalence in the Norwegian general population[6]; over 40% of all cancer patients are believed to suffer from muscle atrophy[8,9]; and there were ~395 million people with TD2M globally in 2010, a number which is expected to double by 2030[10]. Furthermore, in addition to these diseases, sarcopenia – the progressive atrophy of skeletal muscle with advanced age – cost the United States $18.5 billion in 2000. This already substantial cost will only grow, given the projected increase in worldwide sarcopenia prevalence from 50 million people in 2010 to 200 million people by 2050[11]. Despite the severity and the ubiquity of skeletal muscle wasting, no broadly effective skeletal muscle wasting treatments are currently available. Given the financial toll, clinical impact, and ubiquity of skeletal muscle wasting, the absence of available treatments represents a considerable unmet need.

1.2 – Cancer cachexia

Cancer cachexia is specific type of skeletal muscle atrophy wherein cancer patients suffer volumetric skeletal muscle loss, do not respond to anabolic signals, and demonstrate a generally catabolic state[12,13]. As previously mentioned cancer cachexia is observed in 40% of all cancer cases, and is furthermore believed to be indirectly responsible for death in 20% of cancer patients[14,15]. Nevertheless, the molecular underpinnings of the cachectic process have yet to be determined conclusively. Currently, cancer cachexia is thought to occur as a result of a negative energy balance in the patient. This negative energy balance is driven simultaneously by an anorexia-induced reduction in energy acquisition through food, and an increase in energy expenditure due to the increased metabolic demands of tumour(s)[13,16,17]. Tumour cells are able to influence energy expenditure through the inflammatory effects of the cytokines they release, which result in the atrophy of the skeletal muscle. For example the tumour cytokine TNFα activates the NF-κB transcriptional pathway, which results in skeletal muscle atrophy through upregulation of various proteins including the muscle ring finger protein 1 and atrogin-1 ubiquitin ligases[9,18]. The atrophic effects of tumour-secreted factors have been validated to an extent by Sun et al, who observed that treatment of murine muscle cell cultures with tumour-conditioned media (TCM) induced muscle atrophy[19]. In addition to the contribution of the tumour, the administration of chemotherapies can have a deleterious effect on skeletal muscle health[14].

1.3 – Skeletal muscle biology

Human skeletal muscle is composed of cylindrical, post-mitotic, multinucleated, contractile cells called myocytes or myofibers[20]. Within the muscle tissue, myofibers are aligned in the direction of force generation to maximize overall contraction force, and surrounded by an extracellular matrix (ECM) containing collagen IV, laminin, and proteoglycans[21–23]. Each myofiber is composed of myofibrils, which in turn each hold sarcomeres, the contractile units of the skeletal muscle. Large-scale contraction of the skeletal muscle arises from the synchronous sliding of the actin and myosin filaments within each sarcomere[20,24]. A diagram illustrating the components of the skeletal muscle can be seen in Figure 1. Skeletal muscle contraction begins in the neuromuscular junction, the interface between a given motor neuron and the skeletal muscle that it controls. Once activated, the motor neuron releases the neurotransmitter acetylcholine (ACh) into the neuromuscular junction, whereupon ACh binds nicotinic acetylcholine receptors (nAChRs) on

the skeletal muscle[25]. nAChRs are ligand-gated sodium ion channels which open when ACh binds. This allows sodium ions to cross the myofiber membrane, i.e. the sarcolemma, and enter the myofiber and begin a skeletal muscle action potential[25]. The movement of sodium ions into the myofiber depolarizes the sarcolemma, and as a result, calcium ions are released from the sarcoplasmic reticulum into the cytosol. High levels of cytosolic calcium enable myosin filaments to bind and pull on actin filaments, thus producing a muscle contraction[25].
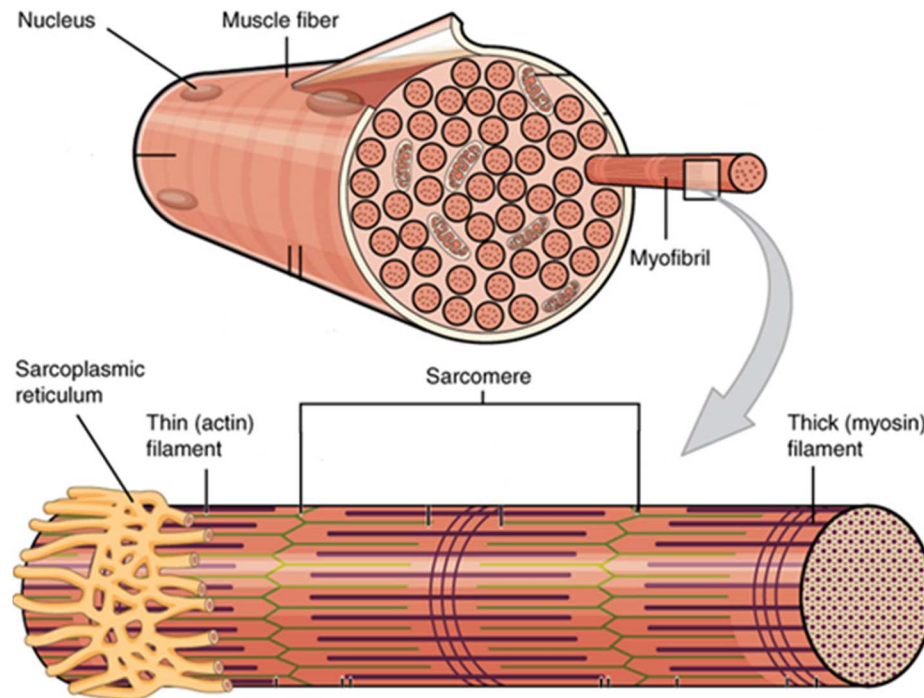
Figure 1. Components and structure of the skeletal muscle. A diagram of the skeletal muscle components, including the muscle fibers, the myofibrils, the sarcomere, and the actin and myosin filaments. Adapted from OpenStax College, 2013[26].

1.4 – Skeletal muscle modeling

When trying to understand a disease or disorder with the eventual goal of drug discovery, the prototypical approach is to conduct research on an *in vitro* model of the body system of interest. In the case of skeletal muscle wasting, this was traditionally done by culturing myofibers on a plastic dish. To produce myofibers *in vitro*, adherent muscle progenitor cells called myoblasts are expanded in cell culture with serum-rich media, and subsequently placed in low-serum media. In

the low-serum environment the myoblasts elongate and fuse with one another, differentiating into myofibers. However, 2D myofiber cultures are markedly limited models of human skeletal muscle. 2D myofiber cultures fail to recapitulate the three-dimensional architecture of human skeletal muscle, they can be difficult to maintain for extended periods due to spontaneous myofiber breakage, and they can only provide imperfect proxy measures of muscle contraction strength, such as myofiber diameter[27,28]. Single-myofiber culture systems are capable of force measurement[29], but these systems are blind to the known impact of the ECM on muscle properties and processes[23,28,30]. To address these shortcomings, a number of groups have worked on engineering 3D skeletal muscle tissues by suspending myoblasts in various biomimetic scaffolds and inducing them to differentiate into myofibers. While these tissues show significant improvement regarding recapitulation of native muscle architecture, weaknesses remain. Some of these groups engineered skeletal muscle tissues from non-human mammalian myofibers[31–35], which are therefore limited in their relevance to human skeletal muscle. Other *in vitro* skeletal muscle tissues have been engineered from human myoblasts, but these tissues were either incapable of any force measurement[36], or relied upon passive force measurements[37]. One group was able to develop 3D skeletal muscle tissues that recapitulated human skeletal muscle biology and functionality to an impressive degree. The tissues were composed of human myoblasts and were capable of measurable contractions that responded to pharmacological intervention in an *in vivo*-like manner[28]. However, the production rate of these tissues was limited – tissues were made using molds that could only generate two tissues at a time. Moreover, while contraction force measurement was possible, it was a laborious process that was invasive and therefore only viable as an endpoint assay. Thus, this tissue engineering method is not ideal for drug screening applications. Conversely, one of the platforms that relied upon non-human skeletal muscle, while inferior from a biological perspective, was relatively high throughput in terms of tissue generation and force measurement. This platform consisted of a plastic 96-well plate where each tissue was anchored to PDMS posts within each well[32,33]. Yet these designs depended upon inexact manual gluing of posts into each plastic well[33], or required several fabrication steps to produce the wells with the capped PDMS posts[32]. Overall, no platform can simultaneously produce human skeletal muscle tissues at a high production rate, enable non-invasive strength quantification of tissue strength, and be fabricated in a single step. The skeletal muscle tissue engineering platforms, which fulfill some of these design criteria, are depicted in Figure 2 and summarized in Table 1. We contend that the lack of available treatments for skeletal muscle wasting is due, in part, to insufficient tools for the study of skeletal muscle and the testing of drugs for muscle effects. The

approval of cerivastatin, a cholesterol-lowering drug that caused fatal muscle side effects and was subsequently recalled[38], provides strong evidence for the inadequacy of these tools.
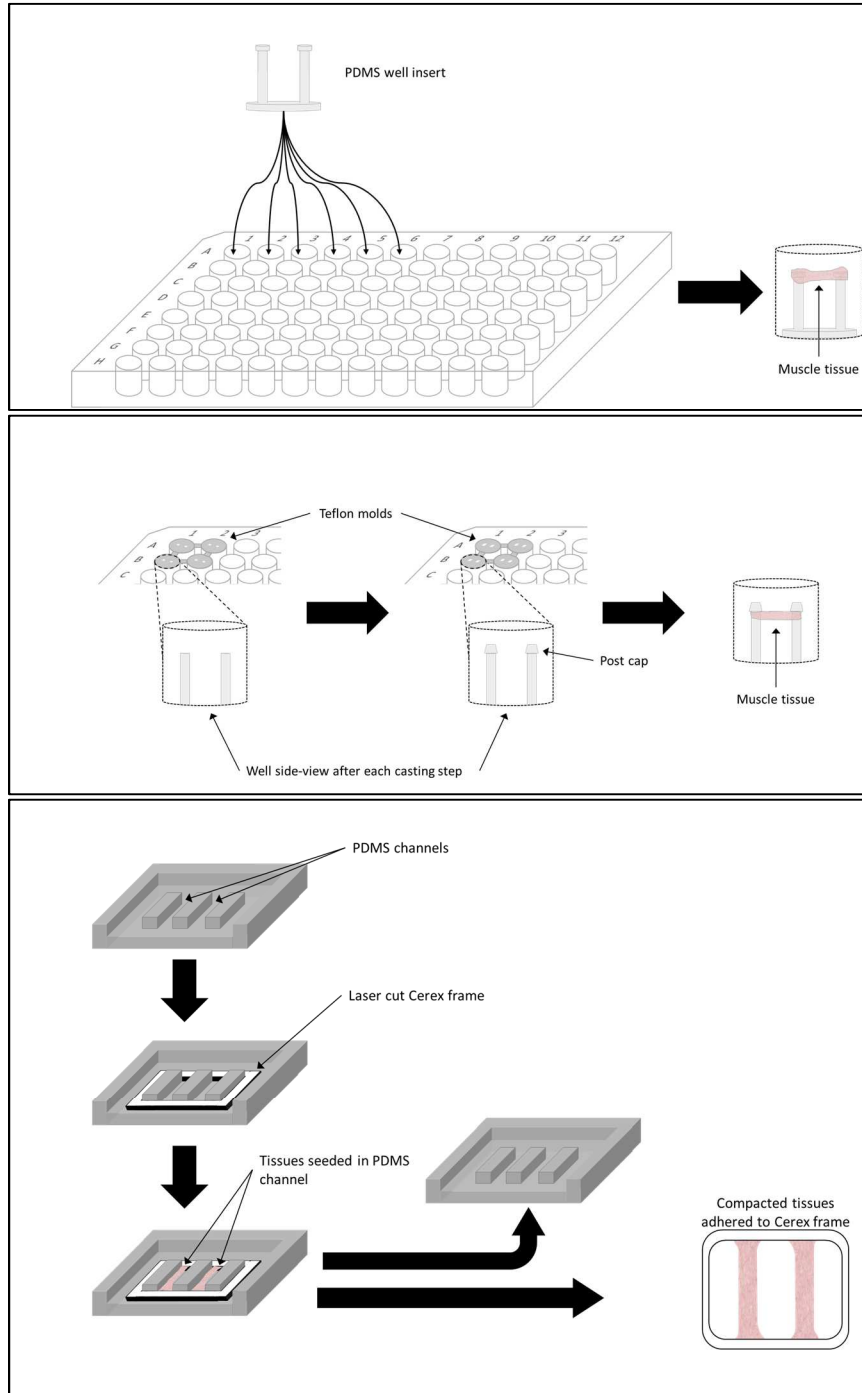
Figure 2. Existing methods for the engineering of skeletal muscle tissues. (A) A schematic illustrating a method to engineer skeletal muscle tissues, as reported by Vandenburgh et al[33]. First, a PDMS microwell insert was fabricated and glued into the wells of a 96-well plate using uncured PDMS. The number of fabrication steps required to fabricate the inserts, the insert fabrication time, and the time for the uncured PDMS glue to cure is not included. After

preparation of the plate, primary mouse myoblasts were suspended in a hydrogel and seeded around posts of PDMS insert. Tissue strength was measured non-invasively through measurement of post deflection. (B) A schematic illustrating a method to engineer skeletal muscle tissues, as reported by Vandenburgh et al[32]. PDMS posts were cast directly inside 96-well plate wells, 4 – 16 wells at a time, using Teflon molds. Actual Teflon mold design was not shown in original paper. Next, PDMS cap structures were cast on the posts in a second casting step. After allowing the plates to cure for at least 6 days after PDMS casting, primary mouse myoblasts were suspended in a hydrogel and seeded in the wells, between the well posts. Tissue strength was measured non-invasively through measurement of post deflection. (C) A schematic illustrating a method to engineer skeletal muscle tissues, as reported by Madden et al[28]. A PDMS mold containing two channels was fabricated with a Teflon mold. Then a laser cut Cerex frame was placed around channels, and primary human myoblasts were suspended in a hydrogel and seeded in the channels. After tissue compaction, the two tissues and the Cerex frame to which they had adhered were removed from the PDMS mold and placed in media. Tissue strength was measured invasively at experimental endpoint, by separating the skeletal muscle tissues from their frame and attaching them to force transducer, then inducing their contraction.

Table 1: Summary of existing muscle tissue engineering platforms and their key characteristics.

Skeletal Muscle Tissue Engineering System Description	Cell Source Species	Cell Density	Tissue Production Rate	Single-step Fabrication?	Ease of Strength Quantification
Cerex-PDMS molds with nylon anchors containing channels for tissue seeding[28]	Human	750,000 cells/tissue	2 tissues per mold	No	Low
96-well plate containing PDMS post well inserts[33]	Mouse	200,000 cells/tissue	96 tissues per plate, after fabrication & gluing of inserts into wells	No	High
PDMS posts casted directly into 96-well plate wells, 4 – 16 wells at a time[32]	Mouse	100,000 cells/tissue	96 tissues per plate, after fabricating posts and caps for 96 wells	No	High

1.5 – Objectives

The objective of this project is to bridge the existing gap regarding the development of treatments for skeletal muscle wasting. This will be done by designing a human muscle microtissue (hMMT) platform that is demonstrably suitable for skeletal muscle biology research and for preclinical drug candidate validation. These overarching goals for the hMMT platform can be conceived of as the sum of several specific criteria:

- The hMMT platform must be capable of generating 3D human skeletal muscle tissues in bulk, and these hMMTs must be representative of native human skeletal muscle.

- The hMMT platform must be easily fabricated, thus encouraging adoption by the wider research community.

- The hMMT platform must provide a non-invasive metric of skeletal muscle strength, thereby enabling simple and relevant assessments of skeletal muscle function.

- The hMMTs generated by the hMMT platform must develop reproducibly, and the mechanical properties of the hMMT platform itself must be consistent.

1.6 – Specific Aims

Specific Aim 1: Fabricate the hMMT platform and assess it for compliance with the aforementioned platform criteria regarding ease of fabrication, consistency of hMMTs and mechanical properties, and non-invasive strength quantification.

Specific Aim 2: Validate that hMMTs are representative of native skeletal muscle by characterizing hMMT development, functionality, and drug response.

Specific Aim 3: Demonstrate utility of hMMT platform by exploring research applications related to cancer cachexia, including modeling cancer cachexia and evaluating chemotherapeutics for myopathic effects.

Chapter 2: Methods

2.1 – Plate fabrication

Fabrication of the custom polydimethylsiloxane (PDMS) 96-well plate which houses the hMMTs was accomplished through sequential fabrication of intermediate plates made of different materials. This was done to minimize wear and tear on the original, 3D-printed plate template. Additionally, using intermediate plates enabled circumvention of fabrication steps wherein plates of a given material are cast from a template made from a material of similar rigidity, as this creates difficulties during product-template separation. The fabrication steps are as follows. First, the original custom plate template was designed in SOLIDWORKS and 3D-printed using a proprietary resin. This 'positive' template is identical to the final product in design, but it is rigid and inflexible. The template was then cast into a flexible PDMS plate using Sylgard 184 silicone elastomer kit (Dow Corning). Liquid PDMS monomer and curing agent were combined in a 10:1 mixture, degassed in a vacuum chamber, and then poured onto the original 3D-printed template, after the template was sprayed with Ease Release® 200 release agent (Smooth-On). A container was used to keep the liquid elastomer in place on top of the template. The template and liquid PDMS were then placed in an isothermal oven at 60 °C and left overnight. The next day, the now cured PDMS plate was manually separated from the template. As a result of the casting process this PDMS plate was a negative mold, i.e. it was three-dimensionally inverted relative to the final product. The negative PDMS plate was then used as a template to cast a positive PDMS plate. Because the template and product were both made of flexible elastomer, corona treatment and 1H, 1H, 2H, 2H-perfluorodecyltrichlorosilane (PDFTS) coating were performed on the template before casting as previously done by Shao et al[39]. This enabled separation of the product from the template after curing. The positive PDMS plate produced by this step was then used as a template for the production of a negative plate made from polyurethane. The polyurethane plate was made by addition of Smooth-Cast® 310 liquid plastic (Smooth-On) to the positive PDMS template. The resultant polyurethane plate was a rigid negative of the final product – the PDMS 96-well hMMT platform. Copies of the hMMT platform were then produced by repeatedly using the polyurethane negative plate as a template. This was done using the same, simple procedure as was used to produce the negative PDMS template from the original 3D-printed template. However, in this case PDMS monomer and curing agent were combined in either a 10:1 or a 15:1 ratio. The

mechanical properties of the posts in the platform wells were measured using a MicroSquisher (CellScale). This instrument uses a high-precision micro-scale actuator to deflect the posts with known amounts of force, while simultaneously measuring the extent of post-displacement.

2.2 – Myoblast isolation from donor muscle tissue

Muscle tissue samples were collected in the form of surgical waste from patients at St. Michael's Hospital in Toronto, Canada receiving elective spinal surgeries. Each donor sample was minced, placed in a gentleMACS™ C Tube, and coated with 7 ml of 0.2 % collagenase in DMEM (Gibco™, from ThermoFisher Scientific). Then, the sample was homogenized 3 times using a gentleMACS™ Dissociator (Miltenyi Biotec) and placed in a 37 °C incubator for 90 minutes to stimulate collagenase-mediated tissue digestion. The sample was then further homogenized by pipetting up and down 15-20 times using a serological pipette. 100 μl of 2 % collagenase and 50 μl of dispase (1.2 U / ml) were then added to the sample, and the sample was returned to the incubator for another 30 minutes of tissue digestion. After this, a syringe was used to run the sample through a 20 G needle 10 times, dissolving the tissue chunks that remained. The resulting sample solution was filtered through a 40 μm cell strainer, centrifuged at 1200 G for 12 minutes, and resuspended in red blood cell lysis buffer. After a 5-minute incubation time, FACS buffer was added to the sample and the solution was centrifuged for 10 minutes at 350 G. At this point the pellet of cells was resuspended in myoblast growth media and plated in a collagen coated cell culture dish. To isolate the CD56$^+$ myoblasts, FACS or the Human CD56 Positive Selection Kit II (EasySep™) was used. In either case, cells were tested in 2D and 3D formats for myofiber formation potential before being used in these experiments.

2.3 – Cell culture

Myoblasts from donor samples were cultured in myoblast growth media containing 79 % Ham's F-10 Nutrient Mix (Gibco™, from ThermoFisher Scientific), 20 % fetal bovine serum (FBS) (Gibco™, from ThermoFisher Scientific), 1 % penicillin/streptomycin, and 5 ng/ml of basic fibroblast growth factor. Immortalized human myoblasts were cultured in 84 % PromoCell Skeletal Muscle Growth Medium, 15 % FBS, and 1 % penicillin/streptomycin. PromoCell Skeletal Muscle Growth Medium contained a supplement mix of epidermal growth factor, fetuin, dexamethasone, and insulin, and 5 % FBS. With the exception of GCaMP6-infected myoblasts and

immortalized myoblasts, all myoblasts underwent no more than 9 passages of expansion before being seeded into hMMTs. MDA-MB-231 triple negative, human metastatic breast cancer cells were cultured to produce tumour-conditioned media (TCM). These cells were cultured in growth media of 90 % DMEM and 10 % FBS. To collect TCM, MDA-MB-231 cells were cultured to 100 % confluency and switched to DMEM-only media. The cells were placed in a 37 °C incubator for 24 hours, whereupon the media was collected and immediately 10X concentrated via centrifugation in 3 kDa Amicon® Ultra-4 Centrifugal Filter Units. TCM filtrate was then 0.2 µm sterile filtered and stored at -80 °C.

2.4 – Human muscle microtissue seeding procedure

To seed the hMMTs, myoblasts were detached from their plates, counted, and centrifuged for 15 minutes at 400 G. The supernatant was aspirated, and the remaining pellet was dissolved in master mix to produce a final cell density of 15×10^6 cells/ml. By volume, the master mix contained 40 % 10 mg/ml fibrinogen solution, 40% DMEM, and 20 % Geltrex™ (ThermoFisher Scientific). Fibrinogen solution was constituted by dissolving fibrinogen from bovine plasma (Sigma) in 0.9 % NaCl and subsequently filtering the solution in a 0.2 µm sterile filter. Thrombin from human plasma (Sigma) was added to the cell suspension at a concentration of 0.2 – 0.5 units of thrombin/mg of fibrinogen. After addition of the thrombin, 15 µl volumes of the cell suspension were quickly pipetted into each of the platform wells (2.25×10^5 cells per well). Each of these 15 ul volumes would eventually become an hMMT. Pipetting was done such that the cell suspension filled the chamber within each well and surrounded the PDMS posts. Then, the seeded cell suspensions were placed in a 37 °C incubator for 5+ minutes, stimulating thrombin-mediated cleavage of the fibrinogen into a fibrin gel. Once the hMMTs had gelled, 200 µl of growth media supplemented with 1.5 mg/ml 6-aminocaproic acid (Sigma) was added to each hMMT. 2 days later, differentiation was induced by replacing growth media with 200 µl of differentiation media. This time point is referred to as differentiation day 0, or day 0. Differentiation media consisted of 2% horse serum (Gibco), 2 mg/ml 6-aminocaproic acid, and 10 µg/ml insulin from bovine pancreas (Sigma) in DMEM. hMMTs were cultured until their experimental end point, with half of the hMMT differentiation media being refreshed every other day. Day 14 was the experimental end point for the majority of hMMTs.

2.5 – Immunofluorescence assays & myofiber diameter measurement

To visualize hMMT myofibers, hMMTs were fixed in 4% paraformaldehyde at room temperature for 15+ minutes. Thereafter, hMMTs were washed three times with PBS, and then simultaneously permeabilized and blocked using a solution of 0.1 – 0.3% Triton-X 100 (BioShop Canada) and 10 – 20% goat serum in PBS. Blocking was done for ≥ 1 hour at room temperature. Primary antibodies were then incubated with the hMMTs for ≥ 3 hours at room temperature, or overnight at 4°C. hMMTs were washed thoroughly and repeatedly with PBS to remove excess primary antibody after which secondary antibodies, nuclear dye, and/or fluorophore-conjugated compounds were incubated with the hMMTs for 0.5 – 1 hour. Excess secondary antibody was removed by three PBS washes, whereupon the hMMTs were ready for fluorescence imaging. Myofiber nuclei were stained using DRAQ5 (Abcam) or Hoechst 33342, while acetylcholine receptors were visualized using α-bungarotoxin-conjugated fluorophore (Invitrogen). Anti-sarcomeric-alpha-actinin (Sigma) antibody was used to visualize myofibers for myofiber diameter measurement. To determine mean hMMT myofiber diameter, confocal image stacks of hMMT immunofluorescence were analysed using ImageJ[40] (NIH). Image stacks were collected along the length of each hMMT, and the diameter of intact myofibers was measured at the centre of each image. These myofiber diameters were averaged to obtain an average myofiber diameter for each image stack and in turn, these image averages were then averaged to determine the mean myofiber diameter for an entire hMMT.

2.6 – Western blot

Multiple hMMTs were extracted from platform wells, flash frozen together in flat-bottom microcentrifuge tubes, and stored at -80°C until protein isolation. To digest hMMTs for protein isolation, a 1:100 mixture of protease inhibitor and RIPA buffer, along with a chrome bead, were added to each microcentrifuge tube containing hMMTs of interest. Each tube was then agitated using a MiniBeadBeater (BioSpec) for 30 seconds. Samples were allowed to incubate for 30 minutes on ice and subsequently centrifuged for 10 minutes at 10,000 G in 4°C to isolate the supernatant. BCA assay (Pierce BCA Protein Assay Kit, ThermoFisher Scientific) was used to determine the protein concentrations. Western blot was conducted using 8% polyacrylamide gels run with a PowerPac™ HC Power Supply (Bio-Rad) for 2 hours, and protein transfer was accomplished using the Trans-Blot® Turbo™ Transfer system (Bio-Rad). Myosin heavy chain

(MHC), MHC-fast, and MHC-slow protein levels were analysed using primary antibodies MF-20, A4.74, and A4.951 respectively (Developmental Studies Hybridoma Bank). Anti-sarcomeric-alpha-actinin (Sigma) and anti-β-tubulin (Abcam) primary antibodies were also used for detection. Anti-rabbit and anti-mouse HRP-conjugated secondary antibodies were used to generate chemiluminescence. SuperSignal™ West Dura Extended Duration Substrate (ThermoFisher Scientific) was used to enhance chemiluminescence, and a ChemiDoc™ XRS+ System (Bio-Rad) was used to visualize protein bands.

2.7 – GcaMP6 myoblast infection

Myoblasts were infected with GCaMP6, an ultrasensitive calcium reporter first reported by Chen et al[41], to assess hMMT functionality. GCaMP6 is a modified green fluorescent protein (GFP) under the control of the myosin heavy chain creatine kinase promoter that fluoresces more strongly in the presence of calcium due to calcium-dependent changes in protein conformation. Myoblast infection was accomplished through initial transfection of GCaMP6 into 293T cells, which assembled and secreted GCaMP6-containing lentivirus into the culture media. Myoblasts were then treated with viral media to enable lentiviral transduction with GCaMP6. FACS was used to sort for GFP fluorescence which identified GCAMP6-expressing myoblasts.

2.8 – hMMT compound screening

Human adult skeletal muscle is composed of fully differentiated, post-mitotic muscle fibers. Consequently, for optimal clinical relevance, screening of compounds must be done on differentiated myofibers rather than myoblast progenitor cells. To that end, treatment of the hMMTs with screening compounds was initiated at the 7th or 8th day of differentiation. However, drug administration methods varied depending on the experiment. For dexamethasone, cerivastatin, and insulin-like growth factor-1 (IGF1) administration, hMMT media was removed on the 7th day of differentiation and replaced with fresh differentiation media supplemented with drug such that the entire hMMT media contained the desired drug concentration. IGF1 levels were maintained via small, daily additions of highly concentrated IGF1.

Dexamethasone/cerivastatin levels were maintained during regularly scheduled ½ media changes. The fresh differentiation media was supplemented with drug such that the half of the hMMT media that was freshly added contained the desired drug concentration. IGF1, cerivastatin, and

dexamethasone drug screens were each performed using hMMTs derived from 3 – 5 donor samples. TCM and irinotecan treatment both began at differentiation day 8. TCM was added to hMMT media daily. Irinotecan was added to hMMTs during regular ½ media changes such that the entire hMMT media contained irinotecan at the desired concentration, or it was added solely on differentiation day 8. DMEM controls were used for cerivastatin, dexamethasone, IGF1, and TCM administrations. A DMSO vehicle control was used for irinotecan treatments.

2.9 – MTT & EdU assays

MTT assays were conducted to assess cytotoxicity of TCM and irinotecan treatment on hMMTs. At day 14, hMMT media was removed and replaced with exactly 100 µl of differentiation media without TCM/irinotecan. 100 µl of differentiation media was also added to an empty hMMT well, which served as a blank control. The hMMTs were left to sit in the incubator for an hour, to allow any metabolic changes induced by the media change to subside. Then, 10 µl were removed from each well and replaced with 10 µl of 5 mg/ml thiazoyl blue tetrazolium bromide (BioBasic Inc). After 2 – 4 hours of incubation at 37°C, 150 µl of 10% SDS in 0.01 M HCl was added to each well, after which the wells were returned to the 37°C incubator overnight. The absorbance of each well was measured with a spectrophotometer the following day. EdU assays were conducted to investigate the persistence of mitotically active cells in hMMTs at different time points after differentiation had been induced. EdU was added to the hMMT of interest at a final concentration of 10 µM at a given time point. The hMMT was then returned to the 37°C incubator for 19 hours, whereupon it was removed from the incubator and fixed in 4% paraformaldehyde for 15+ minutes at room temperature. Next, the hMMT was washed three times in PBS, and then submerged in a permeabilizing and blocking solution of 0.1 – 0.3% Triton-X 100 and 10 – 20% goat serum in PBS. A 1:1000 dilution of Hoechst 33342 was added for half an hour, then washed 3x with PBS. Fluorescence was then assessed using a confocal microscope.

2.10 – Statistical analysis

Statistical analyses were done using Graphpad Prism, $p < 0.05$ was considered significant. Parametric tests performed included one-way and two-way ANOVA. Normality of residuals was checked via Shapiro-Wilk test, while Brown-Forsythe tests were conducted to confirm homogeneity of variances between groups. One-way ANOVA was conducted to assess significance

of drug dose on mean hMMT myofiber diameter, two-way ANOVA was conducted to assess significance of days of differentiation and cell donor on mean hMMT myofiber diameter. Tukey's multiple comparisons post-hoc test was used to identify significant differences between specific levels of each factor. Mann-Whitney U test was conducted to compare force-displacement ratios of hMMT platforms fabricated with different PDMS monomer-curing agent ratios.

Chapter 3: Results

3.1 – hMMT platform is simple to fabricate and capable of bulk hMMT production

To achieve the creation of a tool that is capable of bulk hMMT production, non-invasive hMMT strength quantification, and can be fabricated easily, a production process was developed to generate the hMMT platform – a custom 96-well plate made of flexible PDMS elastomer. The complete hMMT platform fabrication process involved successive casting steps and was nontrivial (Figure 3). However, this production method minimized the number of casting steps involving the original 3D-printed template, thus reducing the likelihood that the 3D-printed template was damaged by a failed casting. Furthermore, with the exception of the second casting step (Figure 3b-c), the hMMT fabrication process was designed to avoid steps wherein rigid molds were used to cast rigid products, or elastic molds were used to cast elastic products, as these steps can result in product feature damage during product-template separation. Crucially while the full hMMT fabrication process is nontrivial, the final casting of the hMMT platform from the rigid polyurethane mold (Figure 3d–e) is a simple, single step and requires neither advanced equipment nor specialized expertise. The sole requirements are PDMS monomer, curing agent, a vacuum pump and vacuum chamber for degassing the PDMS mixture, release agent spray, and an oven. A single polyurethane mold can be reused to fabricate several hMMT platforms. Consequently, once the polyurethane mold has been fabricated, production of 96 hMMTs per day per polyurethane mold becomes possible. Furthermore, because the final fabrication step is simple, the polyurethane molds can be distributed to interested parties who can then easily fabricate hMMT plates for their own research purposes. Thus, fabrication of the hMMT platform is simple enough to encourage adoption by other researchers.
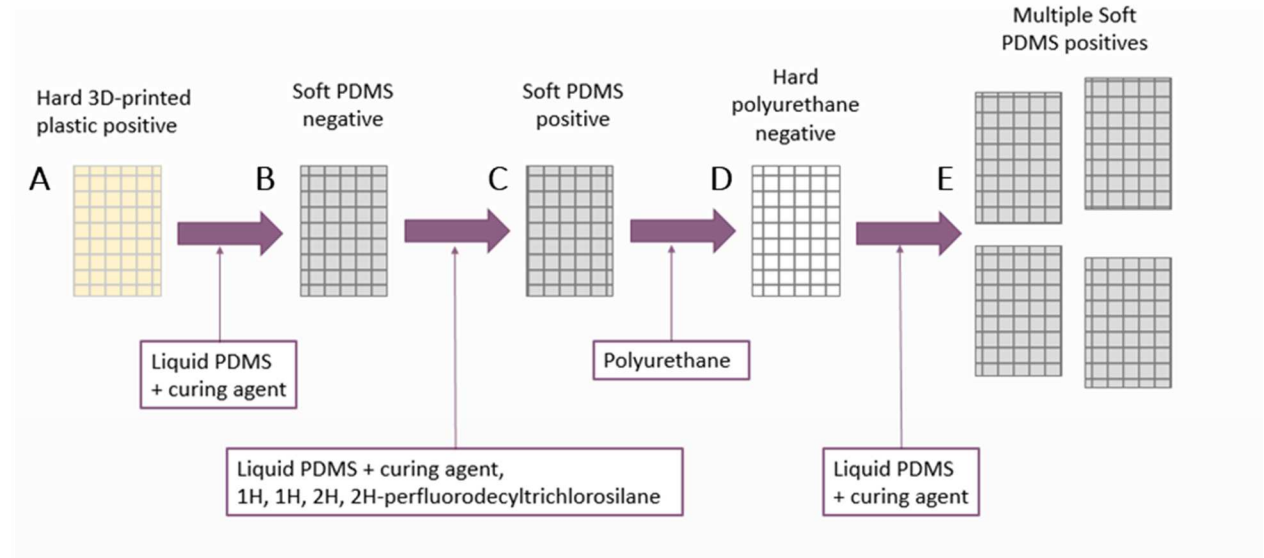
Figure 3. The hMMT platform fabrication process. A schematic of the steps whereby the hMMT platform is produced. (A – B) The first step of the fabrication process. An initial, rigid, 3D-printed positive template was cast into an elastic, PDMS, negative mold via the addition of liquid PDMS monomer and curing agent. (B – C) The second step of the fabrication process. The elastic PDMS negative mold was vapour-coated, and then cast into an elastic, PDMS positive mold via the addition of liquid PDMS monomer and curing agent. (C – D) The third step of the fabrication process. The elastic, PDMS positive mold was cast into a rigid polyurethane negative mold by addition of liquid polyurethane. (D – E) The final step of the fabrication process. The polyurethane mold was used to produce multiple copies of the final product – the elastic, custom PDMS plate that is the hMMT platform.

To generate hMMTs, donated muscle tissue samples were processed and sorted to isolate myoblasts. Myoblasts were expanded in culture and suspended in a fibrin gel, and this suspension was pipetted into the custom wells of the hMMT platform (Figure 4). At the bottom of each well is a 2 mm-deep chamber which holds 2 PDMS posts (Figure 5). The myoblast suspension was

pipetted into this chamber, between and around the posts. The posts provide uniaxial tension to the gel, causing the differentiating myoblasts to self-align between them. The posts are each 2.25 mm tall, are fabricated *in situ* with the rest of the plate, and to serve as tendon-like anchor points for the hMMTs. The elasticity of the PDMS allows the posts to deflect in response to hMMT contraction, and this deflection can be used to assess contraction strength. Arriving at a platform design suitable for the housing of hMMTs required careful consideration of several design criteria and optimization of features. These design elements are listed in full in Table 2, and include post structure, post dimensions, and the 3D-printer model. For example, posts were initially designed to be completely vertical, as seen in Figure 6a. However, hMMTs slid off these posts soon after seeding. To address this issue a sloped segment was added to the top of the posts, which restricted hMMT movement (Figure 6b). After consideration of these design requirements and optimizing the design elements, the hMMT platform could be used to seed hMMTs. As can be seen in Figure 7, the hMMT platform allows generation of several hMMTs simultaneously.
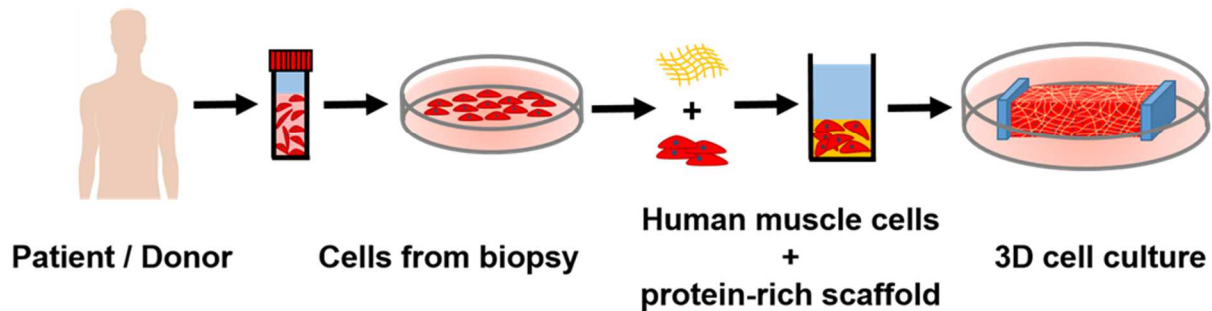
Figure 4: Human muscle microtissue (hMMT) seeding procedure. Schematic of the process whereby a patient muscle sample is used to seed hMMTs. Myoblasts were isolated from human skeletal muscle samples, expanded via cell culture, suspended in a fibrin scaffold, and seeded in the hMMT platform. Schematic modified from Bakooshli & Gilbert, 2015[42], used under CC BY 4.0.
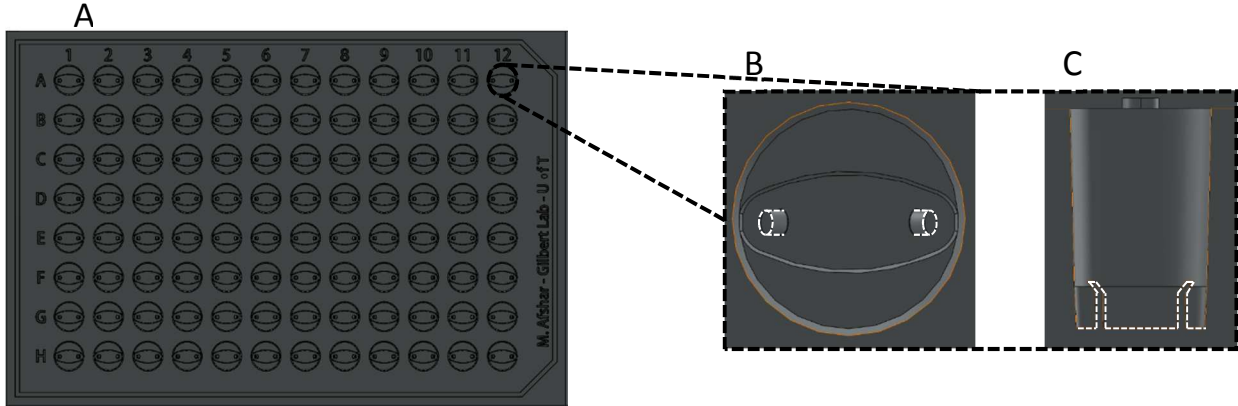
Figure 5. The structure of the human muscle microtissue (hMMT) platform wells. (A) Design schematic of the entire plate. (B) A top-view schematic of the hMMT well. (C) A side-view schematic of the hMMT well.

Table 2: Design elements optimized during the development of the human muscle microtissue platform.

Design Element	Considerations	Selection
Post structure	Column-shaped vertical posts are ineffective at keeping the microtissues anchored in place. Adding a capping structure to the top of the posts will help trap the hMMTs, but will also increase the mass of the posts. Heavier posts are more difficult to deflect for the hMMTs.	A hook-like capping structure was added to the posts. The form of the cap is a slanted segment (slant angle = 51.34°) that only hooks the outer ends of the hMMT. By covering only the outer ends of the microtissue, the cap allows successful casting and does not obscure the hMMT while also firmly securing the hMMTs to the posts.
Shape of post-capping structure	Cap should be as unobtrusive as possible so as not to impair *in situ* imaging of the hMMTs. Caps must also prevent hMMTs from climbing off of the posts, and their shape must allow them to be cast simultaneously with the rest of the plate without breaking.	
Post location	Posts should be placed close enough to each other that the	Posts were placed 3.05 mm from one another, with each

	seeded microtissues fit within a single 4X field of view, thereby facilitating whole-hMMT microscopy. Furthermore, the posts must be located far enough from the sides of the well to accommodate the presence of electrodes for electrial stimulation of hMMT contraction. On the other hand, posts that are too close to one another become unable to exert sufficient tension on the hMMT to stimulate self-alignment of myoblasts.	post being 1.15 mm from the side of the well. This resulted in hMMTs that fit within a single 4X field of view, could be electrically stimulated, and formed from self-aligning myoblasts.
Platform material selection	The material of the platform must be flexible enough to allow post-deflection, and accessible/affordable enough to encourage adoption of the platform by other groups. Importantly, the material must not be autofluorescent, as this would interfere with *in situ* live-image fluorescence microscopy.	Polydimethylsiloxane, a silicone-based elastomer, was selected as the platform material. It is affordable, can be deflected by the hMMTs, and does not demonstrate significant autofluorescence.
Post size	Posts must be large enough to withstand the forces exerted on the plate during product-template separation. Additionally, the posts must be small enough that they are deflected by microtissue contraction, thus enabling strength quantification.	Posts were designed such that post height = 2.25 mm, maximum post width = 0.45 mm, and post thickness = 0.75 mm. Posts survive product-template separation and are deflected by hMMTs.
Ratio of PDMS monomer to curing agent	Curing agent level should be high enough that the PDMS hMMT platform can cure overnight, but low enough that posts are readily deflected by hMMTs.	A PDMS monomer to curing agent ratio of 15:1 was selected.
3D printing process	3D printer model had an appreciable effect on post	3D-printed template was produced by Objex Ltd, using

	fabrication quality, translucence of plate, and adhesion of PDMS to 3D-printed template during casting process.	a Projet MJP 3600 Series 3D printer manufactured by 3D Systems. VisiJet M3 Crystal print material was used.
Well design	hMMT well should guide user while they are seeding the hMMT, reducing the margin for error by helping ensure that the cell suspension properly surrounds the posts.	The base of the hMMT well contains a chamber that is 2.8 mm wide. The hMMT chamber is thus narrower than the base of a typical 96-well plate well, which forces the user to seed the tissue in the appropriate area of the well.
Cell number	Cell number should be minimized to lower the cost of hMMT production. However when seeding cell density is too low, hMMT remodeling is impaired. When seeding cell density is sufficient but seeding volume is too low, the resulting hMMT is unable to withstand the forces of remodeling and breaks.	15×10^6 cells/ml was chosen as the seeding cell density, and a 15 ul seeding volume was used. Thus the final cell number is 225,000 cells/hMMT.
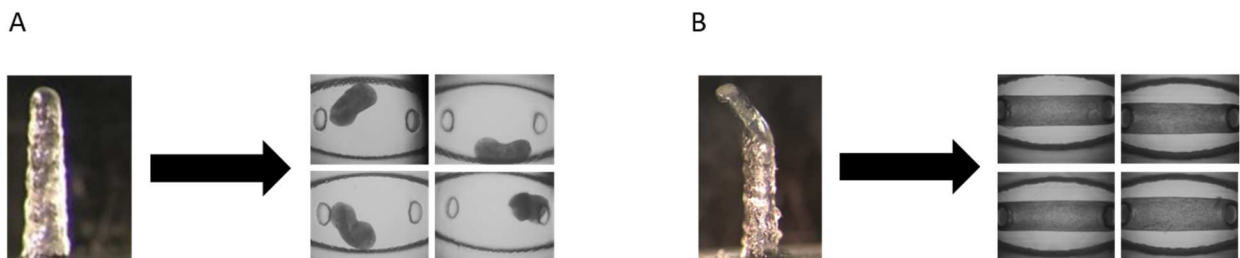
Figure 6. The impact of post design on tissue formation. (A) Image of a post fabricated per the original design, and images of microtissues seeded on posts of this design. (B) Image of a post fabricated per the improved design, and images of microtissues seeded on posts of this design.
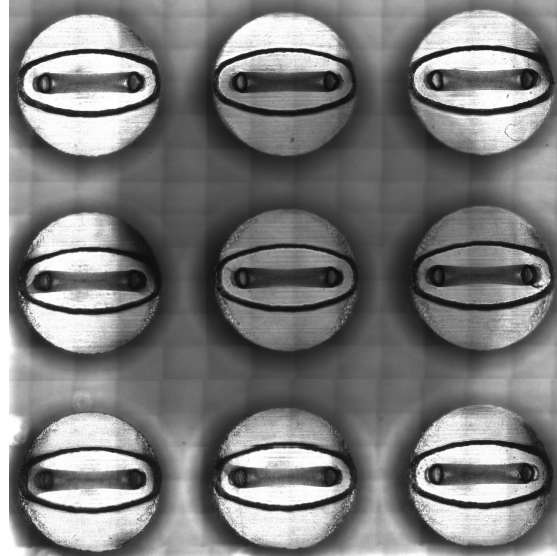
Figure 7. Bulk production capability of the human muscle microtissue (hMMT) platform.
An image of several hMMTs seeded in a single sitting using the hMMT platform.

3.2 – hMMT maturation is reproducible between patients and is consistent with native muscle

hMMT maturation after seeding was studied to characterize the microtissues produced by the hMMT platform, and to compare hMMTs to *in vivo* human skeletal muscle. Examination of hMMT morphology was facilitated by *a priori* platform design considerations regarding hMMT imaging (Table 2). As a result of these considerations, posts were placed close enough to each other that the entire hMMT could be captured in a single field of view, and were designed so as not to obscure the hMMTs from above. The changes in hMMT morphology over time are shown in Figure 8a. At the time of seeding, hMMTs filled the entire chamber in the hMMT platform well. However, hMMTs began decreasing in width soon after seeding. By the time differentiation was induced 2 days after seeding, hMMTs had largely remodeled into a cylindrical shape. From this point onwards, compaction continued but at a much more gradual rate. Next, the hMMT myofiber structural organization underlying this consistent morphology was examined via immunofluorescence. hMMT myofibers were found to align themselves along the length of the hMMT, and they were observed to be multinucleated (Figure 8b). The architectural alignment of

myofibers in hMMTs corresponds closely with that of human skeletal muscle, wherein myofibers are aligned in the direction of force generation and thereby maximize contraction force[21].

To assess the uniformity of hMMT development, both tissue width and myofiber diameter were measured using hMMTs produced from three different donor samples. Figure 8c shows that hMMT width appears to follow a generally consistent pattern regardless of donor sample. Mean tissue width at day 14 of differentiation was 738.5 ± 143.1 µm (mean ± SD). Similarly, mean myofiber diameter also appears consistent regardless of cell donor. Mean myofiber diameter was found to be 12.41 µm, 15.55 µm, and 20.09 µm after 7, 10, and 14 days of differentiation respectively. Two-way ANOVA analysis showed that mean hMMT myofiber diameter increased significantly with increasing days of differentiation (p<0.0001, R^2 = 0.8397), but cell donor had no significant effect on myofiber diameter (p = 0.096, R^2 = 0.0211). The interaction effect between days of differentiation and cell donor was not significant (p = 0.7999, R^2 = 0.0067). Tukey's multiple comparison test further revealed that myofiber diameter at each tested time point was significantly different from all other time points. This finding concords with the visually apparent increase in myofiber diameter with longer differentiation time (Figure 8e). Thus like human skeletal muscle fibers, hMMT myofibers increase in diameter as the hMMT matures[43]. hMMT protein expression was studied during the course of maturation via Western Blot analysis (Figure 8f). hMMTs were found to express muscle-specific MHC and sarcomeric alpha actinin. MHC protein levels increased with increasing differentiation time, while sarcomeric alpha actinin levels remained unchanged. Based on these findings, the hMMT platform produces microtissues that are reproducible with respect to overall morphology and myofiber diameter, throughout the maturation process and regardless of patient donor source. Moreover, the microtissues produced by the hMMT platform demonstrate *in vivo*-like organization of hMMT myofibers, express muscle-specific proteins, and their myofibers thicken as they mature like human skeletal muscle. Thus, the hMMT platform makes hMMTs that are reproducible and resemble human skeletal muscle.
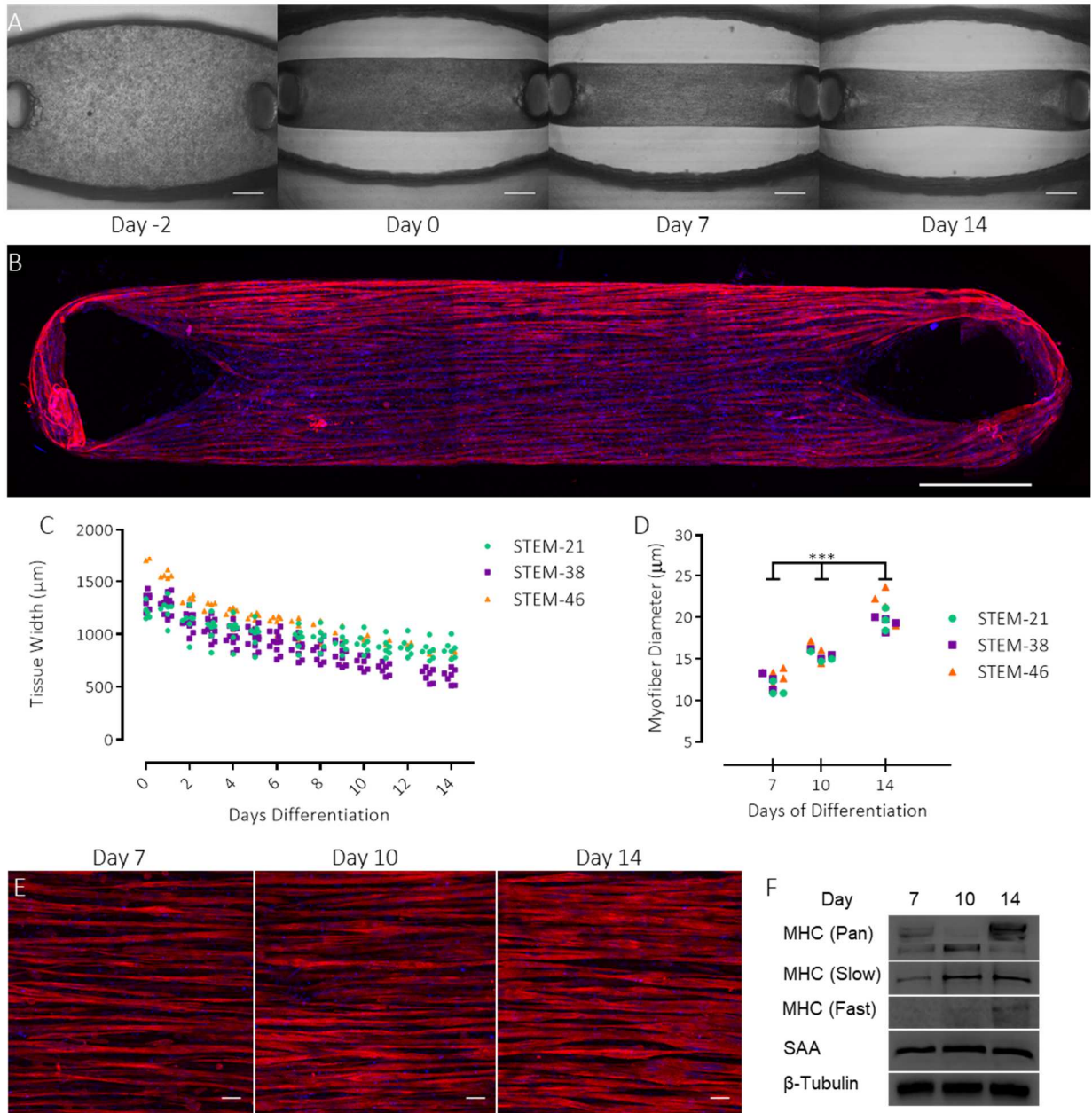
Figure 8. Human muscle microtissues (hMMTs) develop reproducibly, in a manner that resembles native skeletal muscle. (A) Time course of hMMT remodeling over 2 days of growth and 14 days of differentiation. Day -2 refers to the time of seeding, two days before differentiation was induced. Scale bars = 500 μm. (B) Confocal microscopy image of whole hMMT myofiber organization. Scale bars = 500 μm. Sarcomeric alpha actinin shown in red, DRAQ5 nuclear stain shown in blue. (C) hMMT tissue widths during differentiation. Donor source of hMMT cells is indicated by point colour. Mean tissue width at day 14 = 738.5 ± 143.1 μm (mean ± SD). (D) Mean hMMT fiber diameter at day 7, day 10, and day 14 of hMMT differentiation. Statistical significance

was determined by two-way ANOVA analysis and subsequent Tukey's multiple comparison test. (E) Confocal images of hMMT myofibers at different differentiation time points. Sarcomeric alpha actinin shown in red, DRAQ5 nuclear stain shown in blue. Scale bars = 50 μm. (F) An image of a Western blot of muscle marker protein levels in hMMTs after 7, 10, and 14 days of differentiation. MHC = myosin heavy chain, SAA = sarcomeric alpha actinin.

3.3 – hMMTs show *in vivo*-like response to biochemical and physical stimuli

The utility of the hMMT platform rests upon the ability of the hMMTs to accurately recapitulate human skeletal muscle physiology. After establishing that hMMTs exhibit human skeletal muscle structural characteristics and protein expression patterns, hMMTs were assessed to determine whether they could model human skeletal muscle functionality. Given that the central function of muscle is to contract, hMMT functionality was assessed on the basis of contractility. In native skeletal muscle, contraction is induced by acetylcholine activation of nAChRs. Similarly, nAChR presence was confirmed in hMMTs through α-bungarotoxin mediated immunofluorescence (Figure 9a). The functionality of these nAChRs was tested via addition of acetylcholine to hMMT media. 1 – 10 mM ACh induced synchronous hMMT myofiber contraction which visibly deflected the PDMS posts (Figure 9b). hMMTs seeded with myoblasts containing the GCaMP6 calcium reporter demonstrated that the addition of ACh to hMMT media resulted in a rapid cytosolic increase in myofiber calcium levels coincident with hMMT contraction (Figure 10). Thereafter, cytosolic calcium decreased gradually to resting state levels (Figure 10b). This indicates that hMMTs respond to the neurotransmitter ACh by releasing calcium and contracting, mirroring the *in vivo* ACh response.
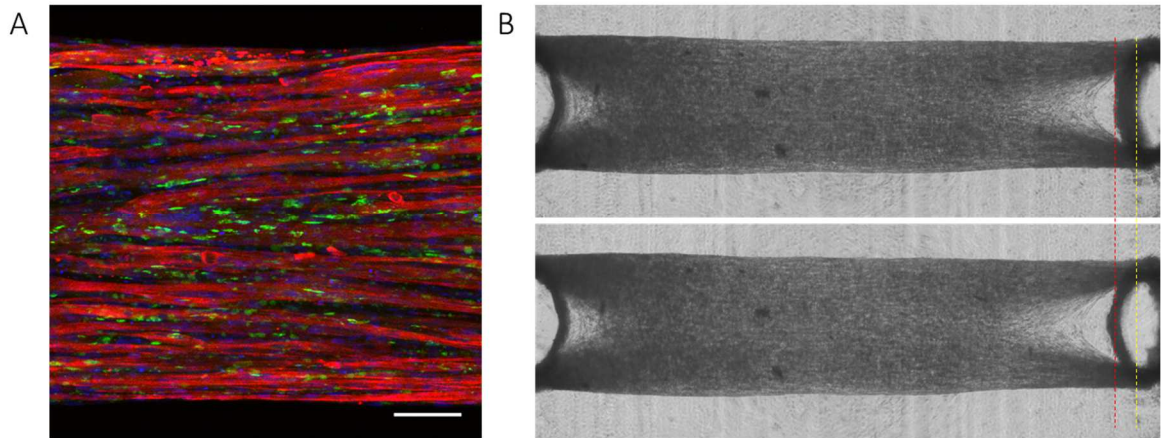
Figure 9. Human muscle microtissue (hMMT) contractile response to acetylcholine. (A) Representative immunofluorescence image of presence of α-bungarotoxin labelled acetylcholine receptors in hMMT myofibers. Sarcomeric alpha actinin is shown in red, Hoechst 33342 is shown in blue, acetylcholine receptors are shown in green. Scale bar = 100 μm. (B) Images of an hMMT before (top image) and during (bottom image) contraction. The dotted reference lines highlight the movement of the posts during contraction.
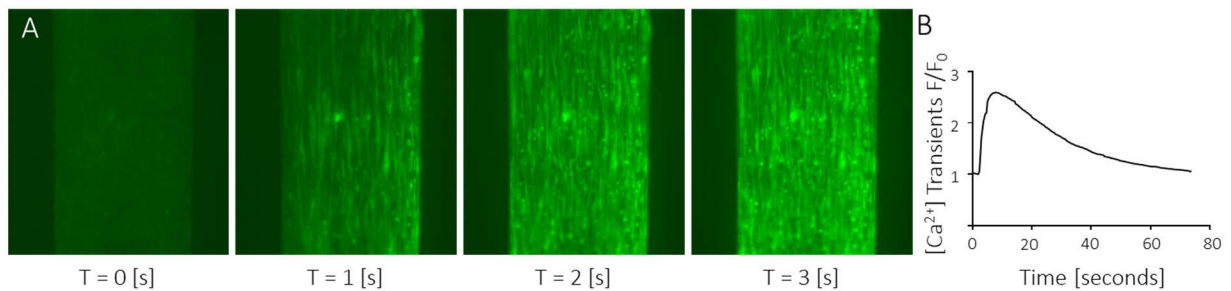
Figure 10. Acetylcholine-induced human muscle microtissue (hMMT) calcium release. (A) Time course of GCaMP6 calcium reporter fluorescence in the seconds after acetylcholine addition to hMMT media to achieve a final concentration of 1 mM. (B) Representative trace of GCAMP6 fluorescence after acetylcholine administration, measured by fluorescence fold change.

To test hMMT response to electrical stimulation, three electrode configurations were tested (Figure 11). Electrical stimulations were performed on hMMTs seeded using immortalized myoblasts from healthy donors. Immortalized myoblast lines were provided by Vincent Mouly's group, who have generated and characterized healthy and diseased immortalized human

myoblast lines previously[44–46]. In Configuration 1, tin wires were placed on opposite sides of the hMMT, in the center of the well, above the hMMT chamber (Figure 11a). The tin wires were connected to a DG1022U Waveform Generator (Rigol Technologies), and application of current induced the calcium-mediated fluorescence associated with hMMT contraction. However unlike ACh stimulation, electrical stimulation was unable to activate all hMMT myofibers (Figure 12a). A review of previous work showed that other groups had opted to stimulate *in vitro* skeletal muscle tissues with an electric field that ran parallel to the length of the myofibers, rather than the perpendicular electric field that our initial configuration produced[32,33,47–50]. To generate an electric field parallel to the length of the myofibers and the hMMT, Configuration 2 was developed. Two 25 G syringe needles were embedded into the floor of the hMMT well chamber, behind the posts. Tin wires were coiled tightly around each of the needles and connected to the Waveform Generator. Current was then applied to produce a 16 V/cm electric field between the needle electrodes (Figure 11a-b). Configuration 2 resulted in synchronous calcium release from all hMMT myofibers, even when using electrical pulses of lower voltage and frequency (Figure 12a-b). It should be noted that in addition to changing the direction of the applied electric field, Configuration 2 placed the electrodes in the hMMT well chamber and thus closer to the hMMT than Configuration 1. Consequently, as a confirmatory test, Configuration 3 was tested, wherein the syringe needles electrodes were placed in the center of the well, inside the hMMT well chamber (Figure 11a). Electrical stimulation using this configuration activated fewer myofibers than Configuration 2, confirming that the key parameter was the direction of the applied electric field relative to the hMMT and myofibers (Figure 12c). Measurement of peak fluorescence fold change also showed that electrical stimulation and ACh administration both elicited hMMT calcium release of similar magnitudes (Figure 13). Based on these findings, hMMTs demonstrate the contractile responses to ACh and electrical stimulation that are seen in *in vivo* human skeletal muscle[25,51–55] and therefore mimic human skeletal muscle functionality. These functionality assessments were enabled by the use of a non-autofluorescent material for the hMMT platform, and the specific placement of the PDMS posts in the hMMT chamber to accommodate the needle electrodes (Table 2).
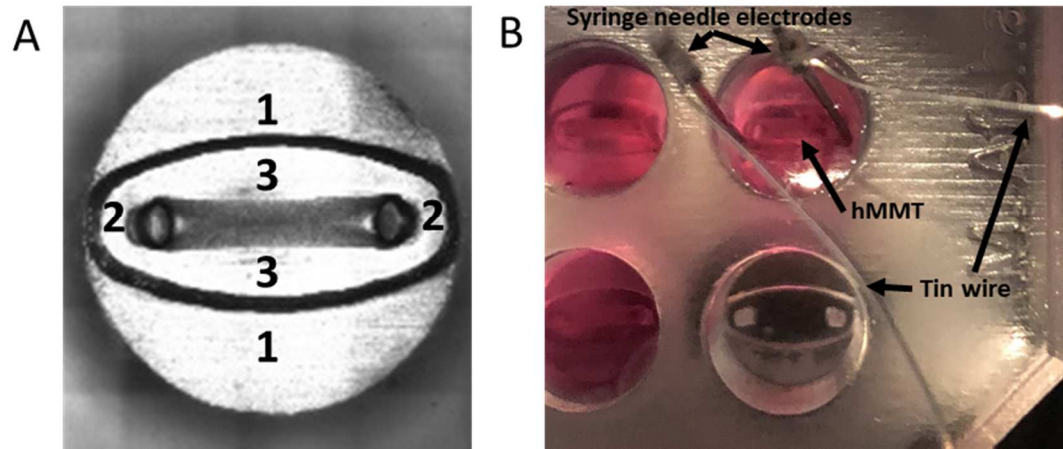
Figure 11. Configurations for electrical stimulation of human muscle microtissue (hMMT). (A) Schematic showing placement of electrodes for various electrical stimulation configurations. Configuration 1 – tin wires are directly placed in the center of the hMMT, above the hMMT chamber. Wire locations are denoted by the number 1. Configuration 2 – 25 G syringe needles electrodes are embedded inside the hMMT chamber, directly behind each post. Needle locations are denoted by the number 2. Configuration 3 – 25 G syringe needles electrodes are embedded inside the hMMT chamber, in the center of the hMMT. Needle locations are denoted by the number 3. (B) Image of Configuration 2 during electrical stimulation. 25 G syringe needles are embedded into the PDMS in the platform well behind the posts of the hMMT.
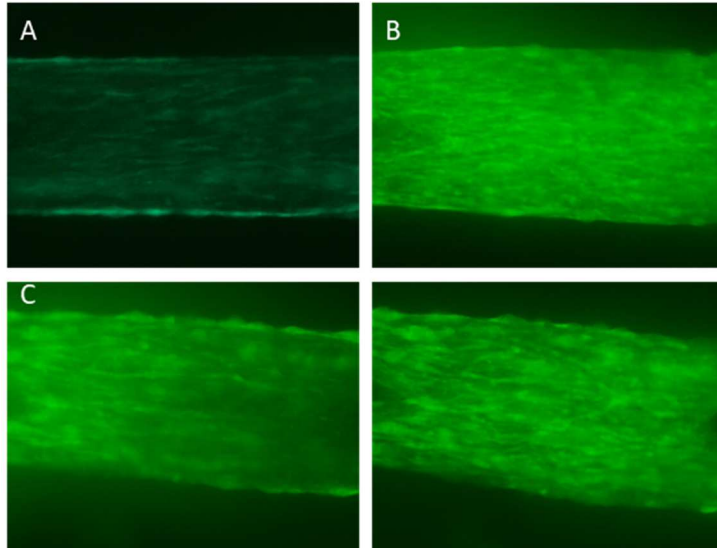
Figure 12. Impact of electrode configuration on human muscle microtissue (hMMT) myofiber calcium release. (A) Peak GCAMP6 fluorescence in a GCaMP6+ hMMT after electrical stimulation using Configuration 1. hMMT had differentiated for 10 days, and was stimulated with a 10 V electrical pulse at a frequency of 10 Hz. (B) Peak GCAMP6 fluorescence in a GCaMP6+ hMMT after electrical stimulation using Configuration 2. hMMT had differentiated for 5 days, and it was stimulated with a 5 V electrical pulse at a frequency of 0.5 Hz. (C) Peak GCAMP6 fluorescence in a single GCaMP6+ hMMT after electrical stimulation using Configuration 3 (left) and Configuration 2 (right). hMMT had differentiated for 7 days, and it was stimulated in both cases with a 5 V electrical pulse at a frequency of 20 Hz.
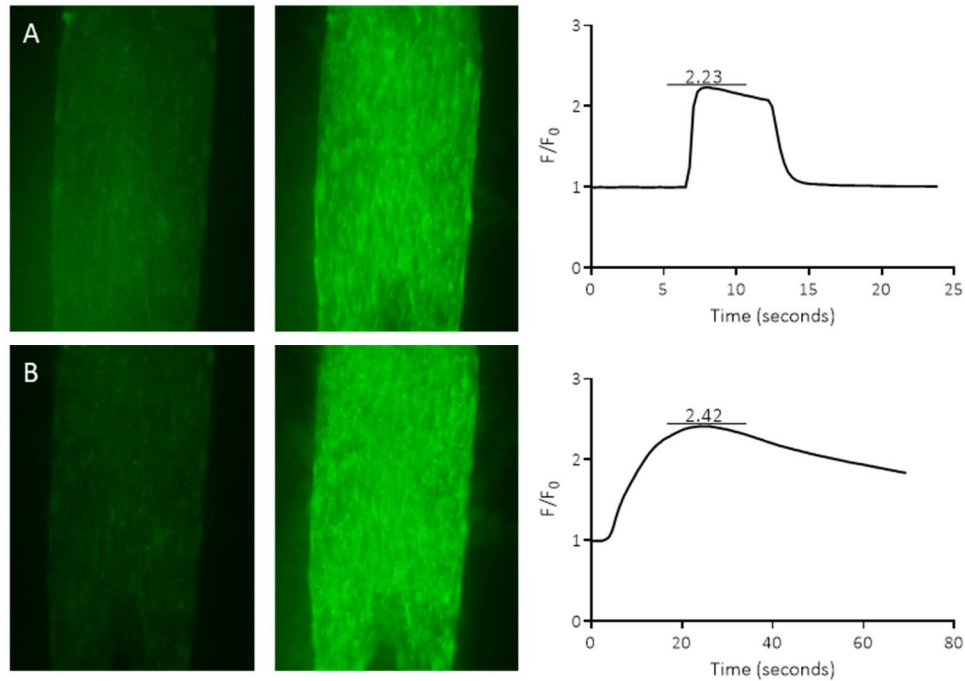
Figure 13. GCAMP6 calcium reporter fluorescence in a single human muscle microtissue (hMMT) after acetylcholine (ACh) and electrical stimulation. (A) Images of a single hMMT before electrical stimulation (left), during peak GCAMP6 fluorescence after electrical stimulation (middle), and a trace of the GCaMP6 fluorescence fold change over time (right). hMMT was stimulated with a 10 V electrical pulse at a frequency of 20 Hz. Max F/F_0 = 2.23. (B) Images of a single hMMT before ACh administration (left), during peak GCAMP6 fluorescence after ACh administration (middle), and a trace of the GCaMP6 fluorescence over time (right). Final [ACh] = 2 mM. Max F/F_0 = 2.42.

3.4 – hMMT drug-response is indicative of *in vivo* drug effects

While hMMTs have been shown to recapitulate structural and functional aspects of human skeletal muscle physiology, drug response is an important indicator of *in vivo* relevance. Validating that hMMTs respond to pharmacological stimuli in an *in vivo*-like manner demonstrates the potential of the model for drug screening applications. The ability of the hMMT platform to identify skeletal muscle toxicity was studied through administration of cerivastatin and dexamethasone. Cerivastatin is an HMGCoA-reductase inhibitor that was found to cause fatal

rhabdomyolysis, a type of myopathy, and subsequently withdrawn from market[38,56]. The precise mechanism of action through which cerivastatin-induced rhabdomyolysis occurs is still unclear[57]. However there is some evidence that concomitant medications and genetic variants are reducing the activity of important drug metabolizing enzymes, thereby impairing cerivastatin clearance[57–60]. Dexamethasone is a glucocorticoid which has been found to improve myoblast differentiation and maturation when added to undifferentiated myoblasts[61–63]. When added to differentiated myofibers, dexamethasone is instead associated with skeletal muscle atrophy, like other glucocorticoids[64–68]. Human skeletal muscle is composed of differentiated muscle fibers. Therefore, to maximize relevance to healthy human muscle, drugs of interest should be tested on myofibers rather than myoblasts. To that end, hMMT drug testing commenced at differentiation day 7, when hMMTs are known to contain myofibers (Figure 8e). hMMTs were found to be sensitive to the atrophic effects of both cerivastatin and dexamethasone. Cerivastatin (Figure 14) and dexamethasone (Figure 15) both caused significant reductions in myofiber diameter. At their highest doses, cerivastatin and dexamethasone treatment induced 43.0% and 43.1% reductions in mean myofiber diameter respectively.
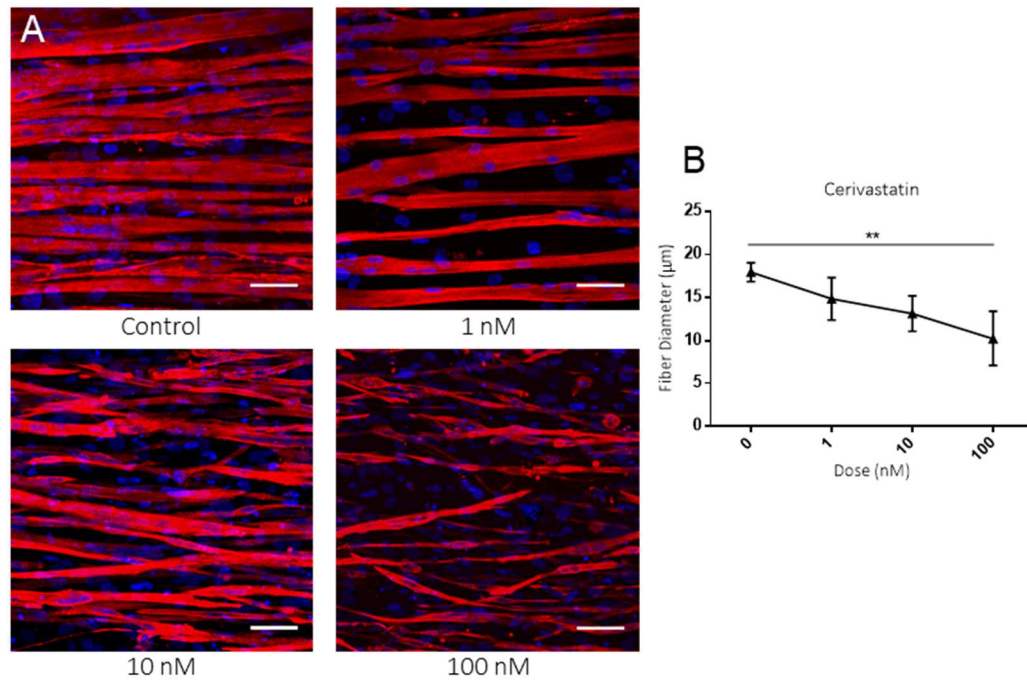
Figure 14. The effect of cerivastatin on human muscle microtissue myofiber diameter (hMMT). (A) Representative images of hMMT myofibers after cerivastatin treatment. Scale bars = 50 μm, sarcomeric alpha actinin containing myofibers shown in red, Hoechst 33342 stained nuclei shown in blue. (B) Plot of mean hMMT myofiber diameter at different cerivastatin concentrations. P = 0.0039. Statistical significance determined by one-way ANOVA and subsequent Tukey's multiple comparisons test.
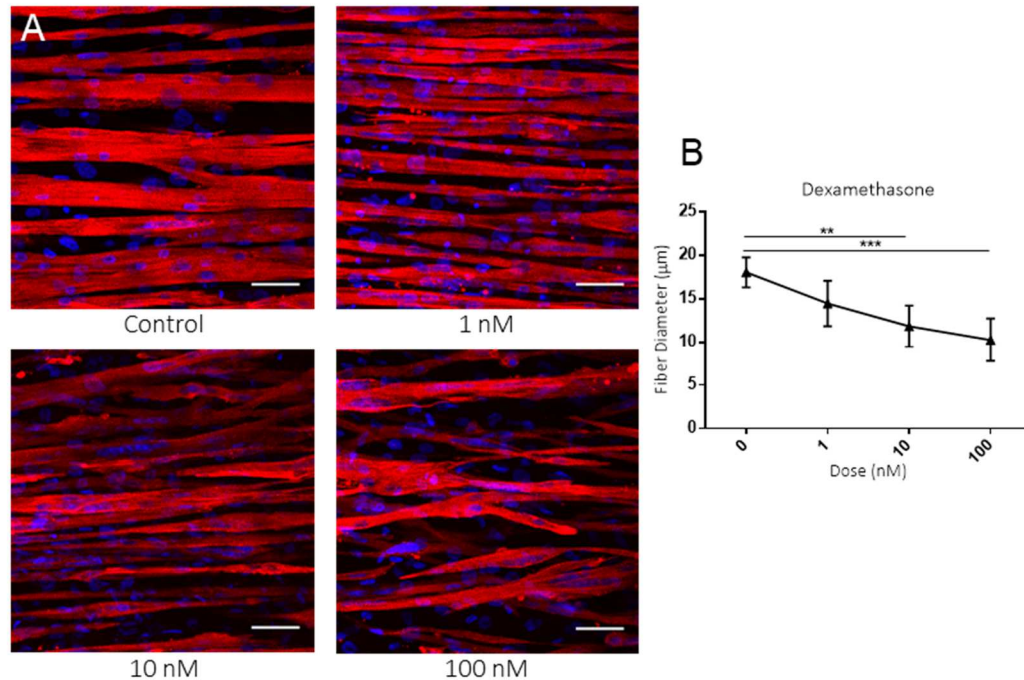
Figure 15. The effect of dexamethasone on human muscle microtissue myofiber diameter (hMMT). (A) Representative images of hMMT myofibers after dexamethasone treatment. Scale bars = 50 μm, sarcomeric alpha actinin containing myofibers shown in red, Hoechst 33342 stained nuclei shown in blue. (B) Plot of mean hMMT myofiber diameter at different dexamethasone concentrations. 0 nM vs. 10 nM: p = 0.0066; 0 nM vs 100 nM: p = 0.0009. Statistical significance determined by one-way ANOVA analysis and subsequent Tukey's multiple comparisons test.

hMMT drug response was also investigated through the administration of Long-R3 IGF1. Long-R3 IGF1 is an IGF1 analog of greater potency, modified to include a glutamine-to-arginine substitution at position 3, and lengthened with the first 11 amino acids in methionyl porcine growth hormone[69]. Unlike dexamethasone and cerivastatin, previous groups have reported IGF1 to foster skeletal muscle hypertrophy in IGF1-overexpressing transgenic mice, as well as in 2D cultures of avian and murine myoblasts[70,71]. Interestingly, IGF1 treatment had no effect on hMMT myofiber diameter at any dose (Figure 16).
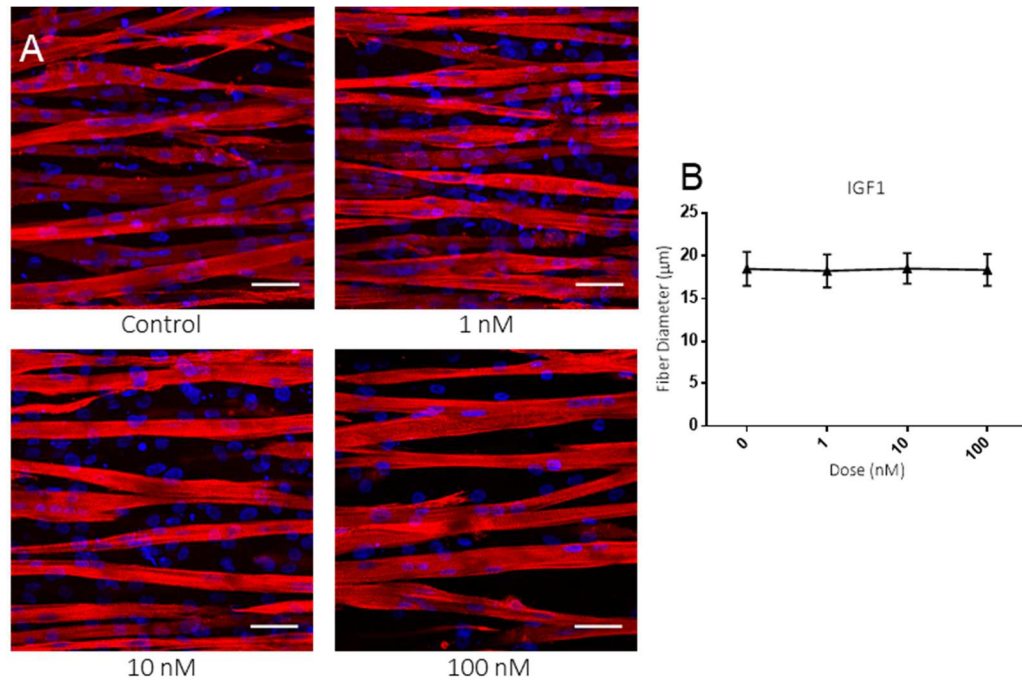
Figure 16. The effect of insulin-like growth factor 1 (IGF1) on human muscle microtissue myofiber diameter (hMMT). (A) Representative images of hMMT myofibers after IGF1 treatment. Scale bars = 50 μm, sarcomeric alpha actinin containing myofibers shown in red, Hoechst 33342 stained nuclei shown in blue. (B) Mean hMMT myofiber diameter at different concentrations of IGF1.

3.5 – Non-invasive hMMT strength quantification

After development of the hMMT platform and characterization of hMMT biology and functionality, the non-invasive strength quantification capabilities of the platform were studied. First, the amount of force needed to deflect the PDMS posts was investigated. Posts were excised from a fabricated hMMT platform and analysed with a MicroSquisher, which yielded a standard curve of force vs. post-displacement. Post-displacement was measured at the tip of the posts, where the hMMTs are expected to be. The standard curves generated by the MicroSquisher data can be seen in Figure 17. The slopes of the standard curves represent the force-displacement ratio of the posts, i.e. the micrometres of post displacement caused by a single micronewton of force. Posts were tested to determine the forces needed to achieve between 0 and 400 μm of PDMS post deflection, and it yielded an average force-displacement ratio of 4.52 ± 0.79 μN/μm. R^2 > 0.99 was

observed for all wells tested, indicating a consistently linear relationship between force and post displacement. Within the bounds of the tested displacement magnitudes, the force-displacement ratio can be used to determine hMMT contraction strength from hMMT-induced post-displacement. In this way the hMMT platform enables non-invasive quantification of hMMT strength, by measuring post displacement alone. A MATLAB image analysis algorithm was developed to further accelerate the strength quantification process. The algorithm takes a video of an hMMT contraction as input, and then returns the maximum post displacement achieved by the contraction. Contraction videos were recorded using an iPhone 5 (Apple) with a LabCam Microscope Adapter for iPhone 5S/SE (iDu Optics). Figure 18a-c demonstrates the MATLAB algorithm image recognition.
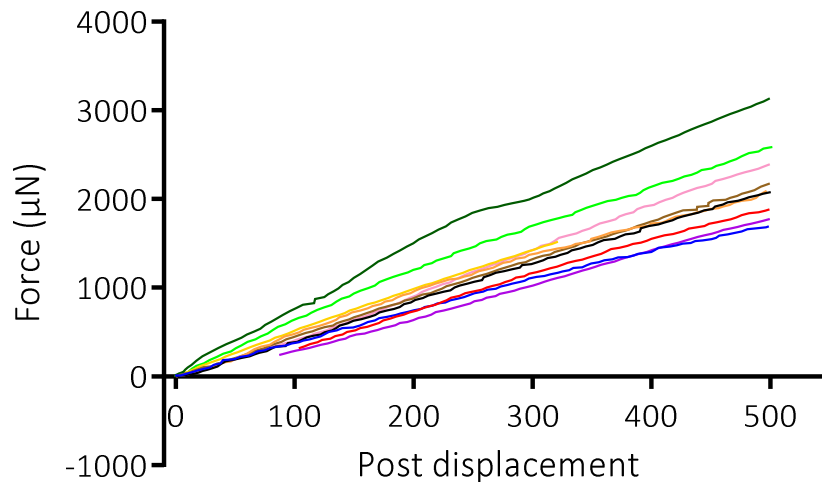
Figure 17. Standard curve of force vs. post displacement for each PDMS post tested. A plot depicting the force-displacement ratio for each post (n = 10) tested. The slope of each curve indicates that post's force-displacement ratio, i.e. the amount of force required to displace the post by 1 μm. Mean force-displacement ratio = 4.52 ± 0.79 μN/μm (mean ± SD), mean R^2 = 0.997.
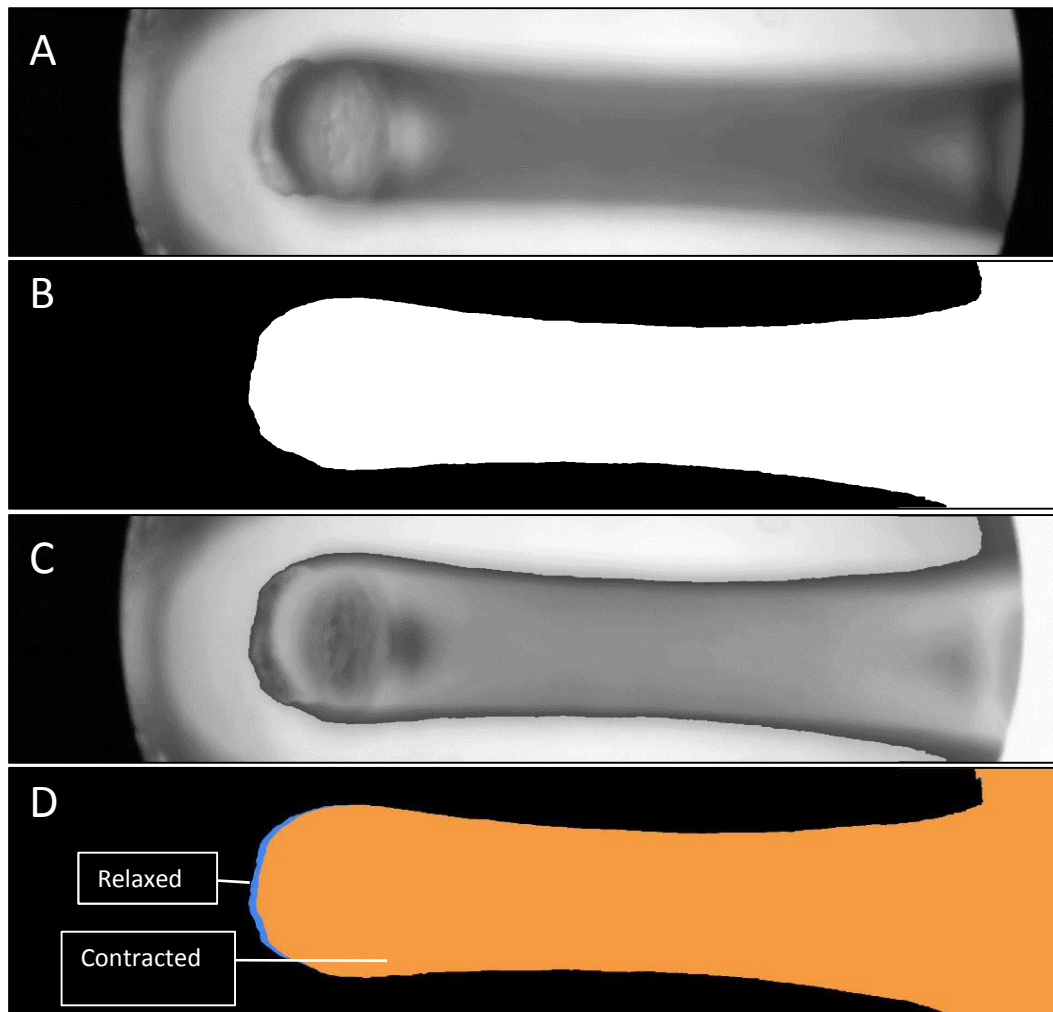
Figure 18. MATLAB image analysis. (A) Still image from a video recording of a microtissue contraction. (B) MATLAB tissue recognition. Recognized object is shown in white. (C) Overlay of original image and MATLAB-recognition. Black outline shows region of MATLAB-recognition. White texturing shows original image. (D) Image showing the extent of hMMT post-displacement. The blue trace represents hMMT position before contraction, while the orange shows the hMMT at the peak of its contraction.

Despite the substantial successes of the hMMT platform, two key limitations persist. First, hMMT-mediated post deflection has thus far been weaker than desired (Figure 18d), and second, even this slight degree of hMMT-mediated post deflection has been inconsistently demonstrated. To address the first limitation and increase the extent of hMMT-mediated post deflection, two approaches were taken. The first was to decrease the size of the posts, thereby reducing the force

needed to deflect them. However, this strategy was unsuccessful. As alluded to in Table 2, reducing the dimensions of the posts made them unable to remain intact throughout the casting process. The second approach was to reduce the stiffness of the posts by modulating the composition of the PDMS elastomer (Table 2). Per manufacturer instructions, PDMS is typically[32,33,39] produced by making a 10:1 mixture of PDMS monomer to curing agent. This ratio was used to make the initial plates, but to reduce post stiffness the level of curing agent was decreased to a 15:1 mixture of PDMS monomer to curing agent. Wells cast using this modified mixture were sent for MicroSquisher analysis and compared to the previous MicroSquisher results. Changing the composition of the PDMS was found to have a significant effect, causing a 55% decrease in median force-displacement ratio (4.32 vs. 2.33 p < 0.0001) (Figure 19). Nevertheless, post deflections induced by hMMT contractions were still quite small. The second limitation, the inconsistency in the ability of the hMMTs to deflect the posts to any degree, was found to vary significantly from tissue to tissue and even from post to post within the same tissue. Furthermore, variation in force-displacement ratios was observed in MicroSquisher analysis of the posts (Figure 17). The inconsistent force-displacement ratios in particular suggested a flaw in the fabrication of the plates, rather than an issue with the homogeneity of the hMMTs. Upon close examination, the presence of artifacts along the lengths of the PDMS posts was observed (Figure 20a). These artifacts appeared to inhibit the upwards migration along the posts that hMMTs demonstrate as they mature. Because the degree of post deflection is dependent on the height of the hMMTs on the posts[32], inhibiting the upwards migration of the hMMTs would necessarily impair hMMT-mediated post deflection. Thus, these artifacts are likely contributing to the weakness of the hMMT-mediated post deflections. As can also be seen in Figure 20a, artifact size and abundance vary from post to post. Consequent post-to-post differences in post size and structure therefore explain the post-to-post differences in force-displacement ratio. Furthermore, the variations in PDMS artifact levels between posts resulted in posts which differentially inhibited hMMT migration to the top of the posts. The resulting disparities in hMMT post height likely also contributed to the observed inconsistencies in hMMT-mediated post deflections. In Figure 20b, the right post allows upwards migration of the tissue while the left post prevents tissue migration. Consequently, a single contraction would cause a smaller post displacement in the left post than the right post. Several modifications to the post design and fabrication process

have been attempted to eliminate or reduce the presence of the artifacts on the posts. Testing of these designs is still ongoing.
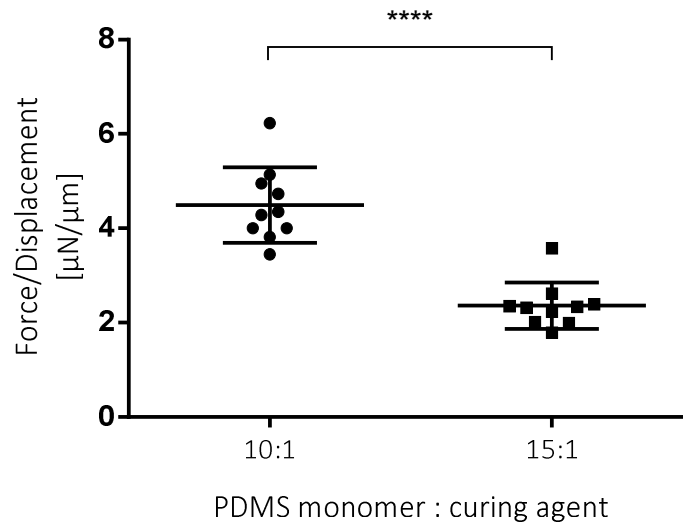
Figure 19. The impact of polydimethylsiloxane (PDMS) composition on force-displacement ratio. A scatterplot displaying force-post displacement ratio in wells made from a 10:1 mixture (n = 10) and 15:1 mixture (n = 10) of PDMS monomer and curing agent. Median force displacement ratios: 4.32 vs. 2.33; p < 0.0001 by Mann-Whitney U Test.
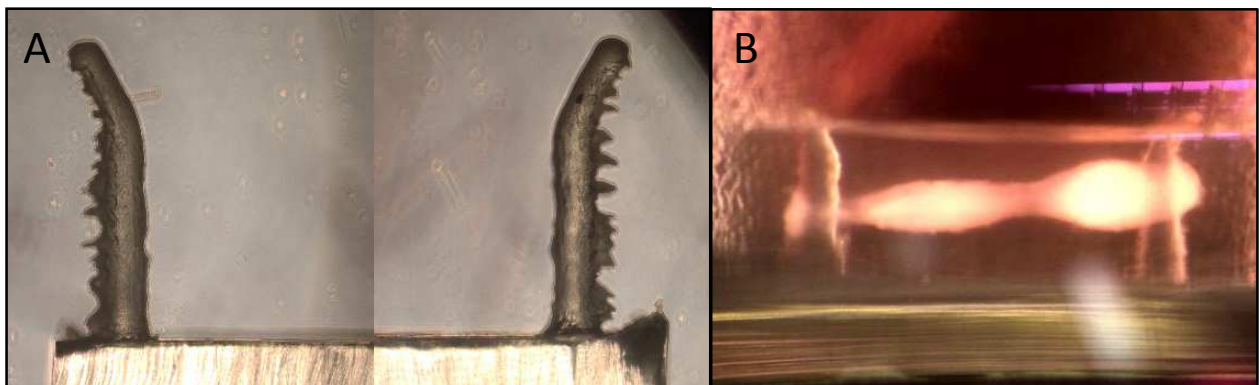
Figure 20. Platform fabrication issues. (A) An image of PDMS artifacts on the post. (B) An image of a microtissue, showing tissue height differences between posts.

3.6 – hMMT platform supports modeling cancer cachexia, and identifies chemotherapeutic toxicity in skeletal muscle

As a tool to facilitate skeletal muscle tissue engineering, the primary purpose of the hMMT platform is to enable users to answer physiological questions, be they related to endogenous processes or drug toxicity. Thus, potential applications of the hMMT platform were preliminarily explored with respect to cancer cachexia.

The etiology of cancer cachexia is still poorly understood, but existing research attributes cancer cachexia skeletal muscle wasting at least partially to the inflammatory effects of tumour-secreted factors[72-75]. Given the considerable degree of uncertainty regarding cancer cachexia, a model of cachectic skeletal muscle would be highly beneficial. Such a model could potentially enable cachexia drug screening, or to facilitate research of cancer cachexia pathobiology. With this in mind, we adapted the hMMT platform to serve as a model of cancer cachexia. MDA-MB-231 triple negative metastatic breast cancer cells were expanded in culture and allowed to condition DMEM media. This TCM was then concentrated and administered to hMMTs. Preliminary results suggested that TCM administration damaged hMMT myofibers, recapitulating the skeletal muscle atrophy seen in cachectic breast cancer patients[76] (Figure 21). However, this toxicity did not go so far as to impair mitochondrial activity, as an MTT assay did not reveal significant differences in metabolism (Figure 22a).
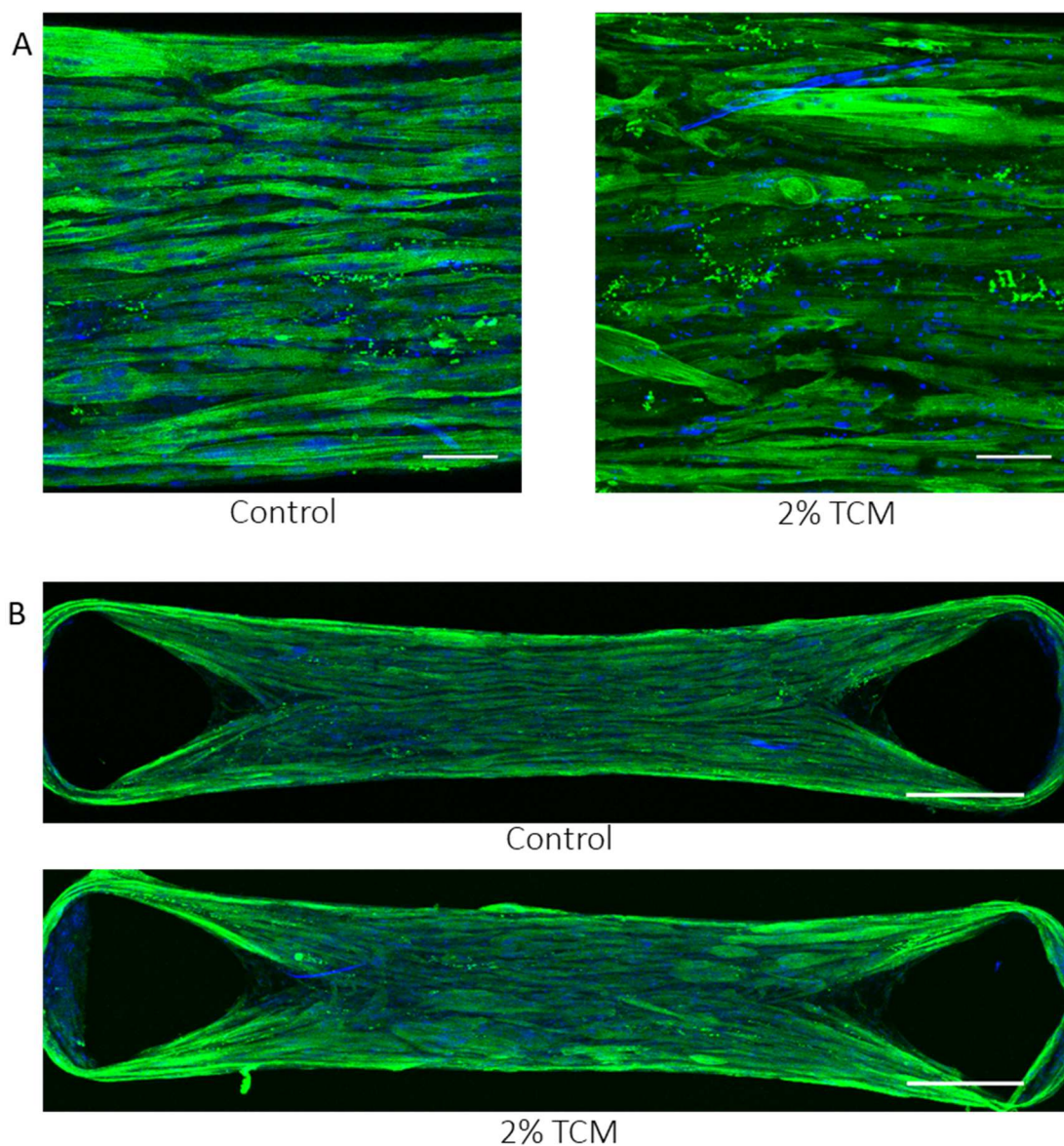
Figure 21. Tumour-conditioned media (TCM) effect on human muscle microtissue (hMMT) myofibers. (A) 20X confocal microscopy images of hMMTs fixed on differentiation day 14 after treatment with DMEM or 2% TCM. (B) 4X confocal microscopy images of hMMTs fixed on differentiation day 14 after treatment with DMEM or 2% TCM. Scale bars = 50 μm (top images) and 500 μm (whole hMMT images); sarcomeric alpha actinin shown in green, Hoechst-stained nuclei shown in blue.
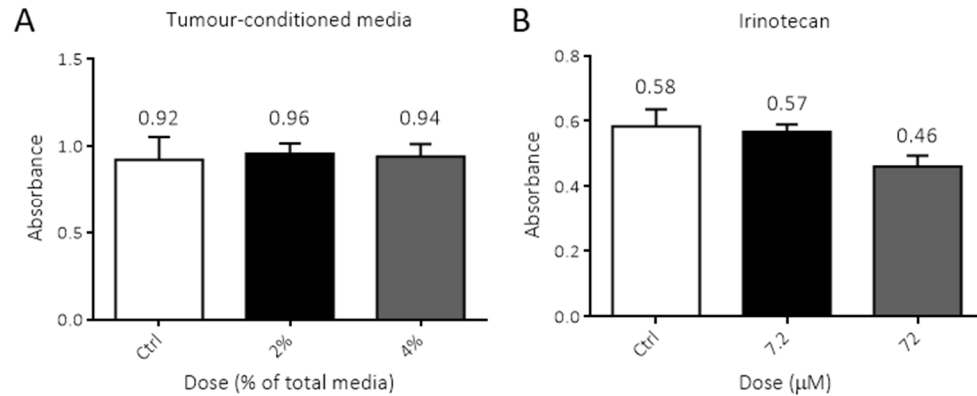
Figure 22. MTT assay results after human muscle microtissue (hMMT) treatment with tumour-conditioned media (TCM) and irinotecan administration. (A) Graph of MTT absorbance in hMMTs dosed with 0%, 2%, or 4% TCM. (B) Graph of MTT absorbance in hMMTs treated with increasing doses of irinotecan.

Although chemotherapy is often acknowledged as a potential causative factor for cachexia, the bulk of cancer cachexia research focuses on the contribution of the tumour to skeletal muscle atrophy[77,78]. Nevertheless certain chemotherapies, such as doxorubicin[79–83] and vincristine[84,85], are known to be myopathic. To illustrate a potential drug screening application, the hMMT platform was used to screen the chemotherapies gemcitabine and irinotecan for atrophic effects. These treatments were specifically chosen as they are indicated for pancreatic cancer, one of the most strongly cachexia-associated cancers[14,86,87]. Recent studies have found that 5 weeks treatment with a regimen containing irinotecan and two other chemotherapies caused muscle atrophy and mitochondrial depletion in mice[88], and administration of irinotecan alone to C2C12 myotubes induced cell death[89]. Despite these findings, it is still unclear whether irinotecan-mediated toxicity extends to human muscle fibers aligned in a thick tissue-like structure. Gemcitabine monotherapy has only been shown to be atrophic in rare clinical cases[90–94]. hMMT myofibers appeared unaffected by a preliminary administration of gemcitabine, where gemcitabine was added on differentiation day 8, differentiation day 10, and differentiation day 12 (Figure 23). Conversely, irinotecan administration on differentiation days 8, 10, and 12 caused severe ablation of myofibers (Figure 24) and increasing irinotecan dose was coincident with a downward trend in metabolic activity (Figure 22b). To more closely imitate a chemotherapy treatment regimen, wherein chemotherapy is given intermittently[95], hMMTs were given a one-time irinotecan dose at

differentiation day 8. After the irinotecan administration, half of the hMMT media was changed every other day until differentiation day 14. Again, irinotecan caused myofiber degradation. Examination of hMMT myofibers shows that this reduced irinotecan administration schedule still caused a dose-dependent decrease in myofiber diameter (Figure 25). The observation that hMMT myofibers are apparently insensitive to gemcitabine but degrade in response to irinotecan illustrates that hMMT atrophy is selective for myopathic compounds.
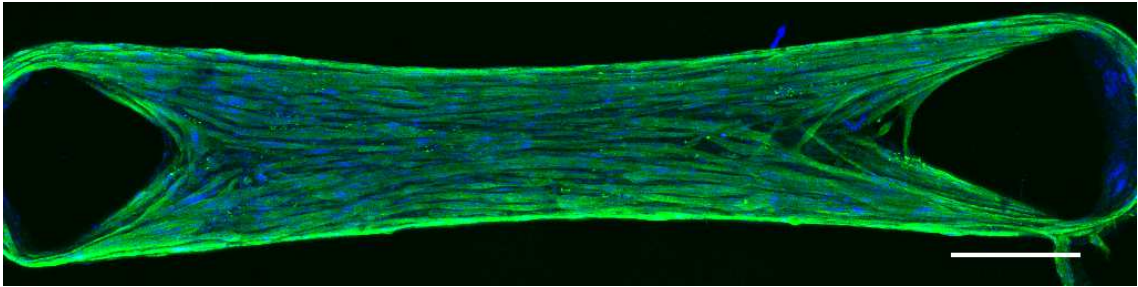
Figure 23. Effect of gemcitabine on human muscle microtissue myofibers. An hMMT fixed on differentiation day 14 that has undergone treatment with 320 µM gemcitabine. Scale bars = 500 µm; sarcomeric alpha actinin shown in green, Hoechst-stained nuclei shown in blue.
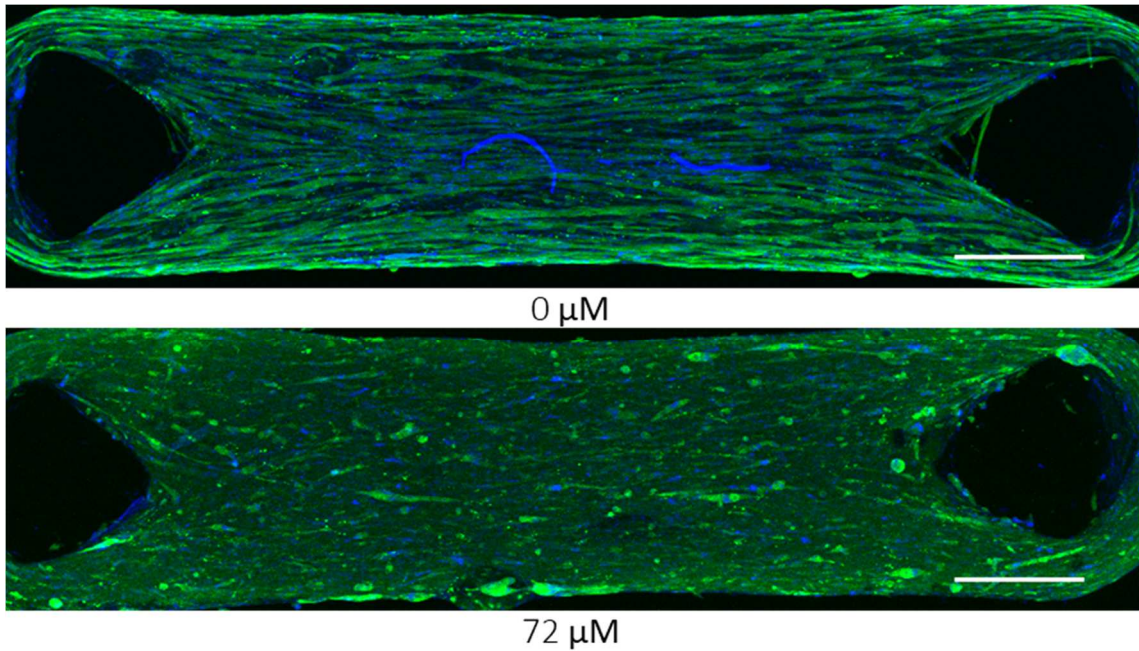
Figure 24. Impact of irinotecan treatment on human muscle microtissue (hMMT) fibers. Confocal fluorescence images of a control and irinotecan-treated hMMT fixed on differentiation day 14. Scale bars = 500 μm; sarcomeric alpha actinin shown in green, Hoechst-stained nuclei shown in blue.
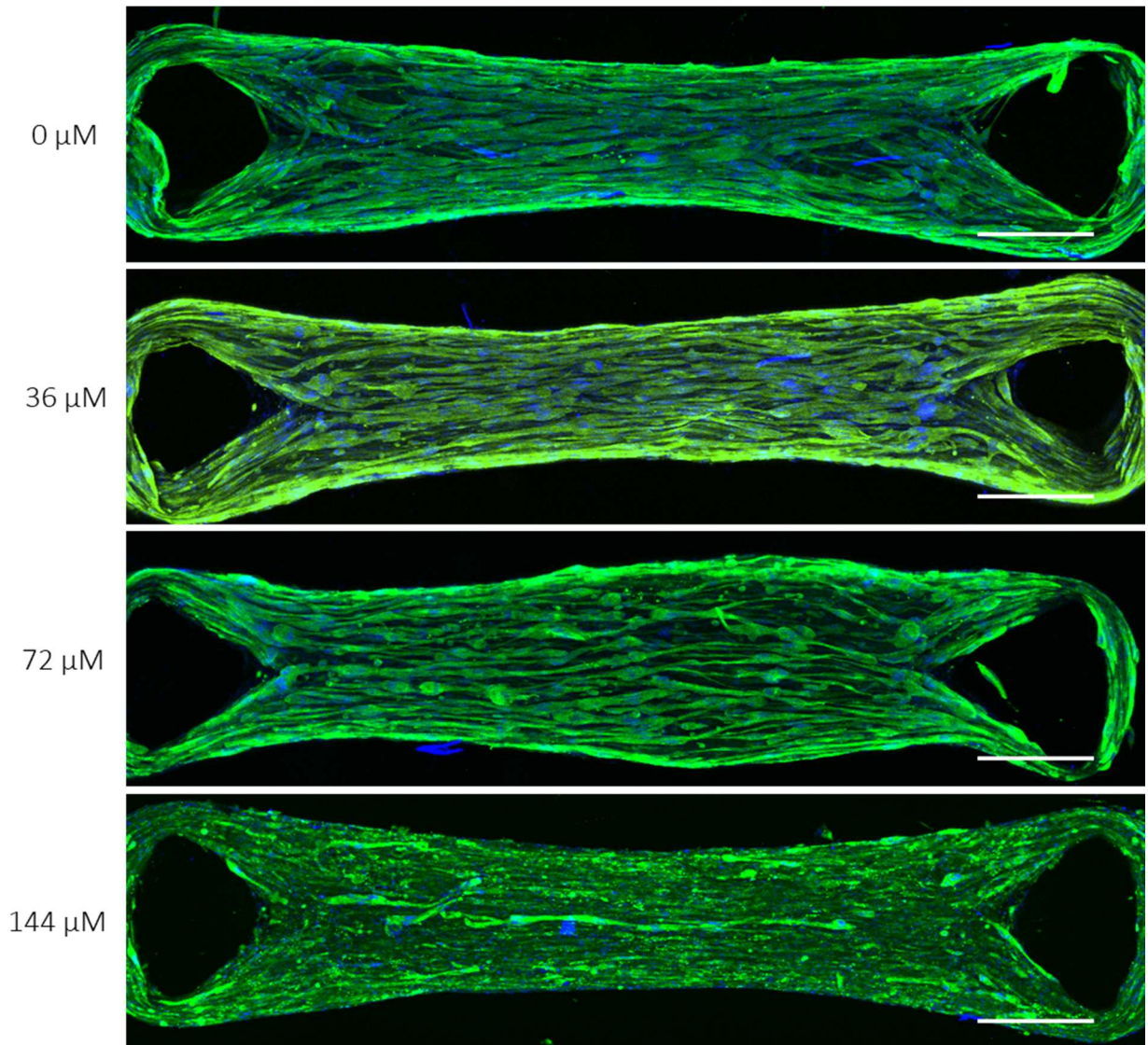
Figure 25. Effect of single-dose irinotecan treatment on human muscle microtissue (hMMT) myofibers. Confocal fluorescence images of day 14 hMMT myofibers after a single administration of irinotecan on day 8. Scale bars = 500 µm; sarcomeric alpha actinin shown in green, Hoechst-stained nuclei shown in blue.

Gemcitabine is a cytidine analogue, which inhibits chain elongation during DNA replication[96], while irinotecan is a topoisomerase I inhibitor, causing apoptosis of replicating cells[97]. Given their mechanisms of action both chemotherapies should have no effect on the post-mitotic cells of the skeletal muscle. To confirm that the observed irinotecan toxicity was not due to the persistence of mitotic hMMT cells, an EdU assay was conducted. While chemotherapy treatment began at

differentiation day 8, EdU assay results confirm that the vast majority of hMMT cells were post-mitotic at this time point (Figure 26).
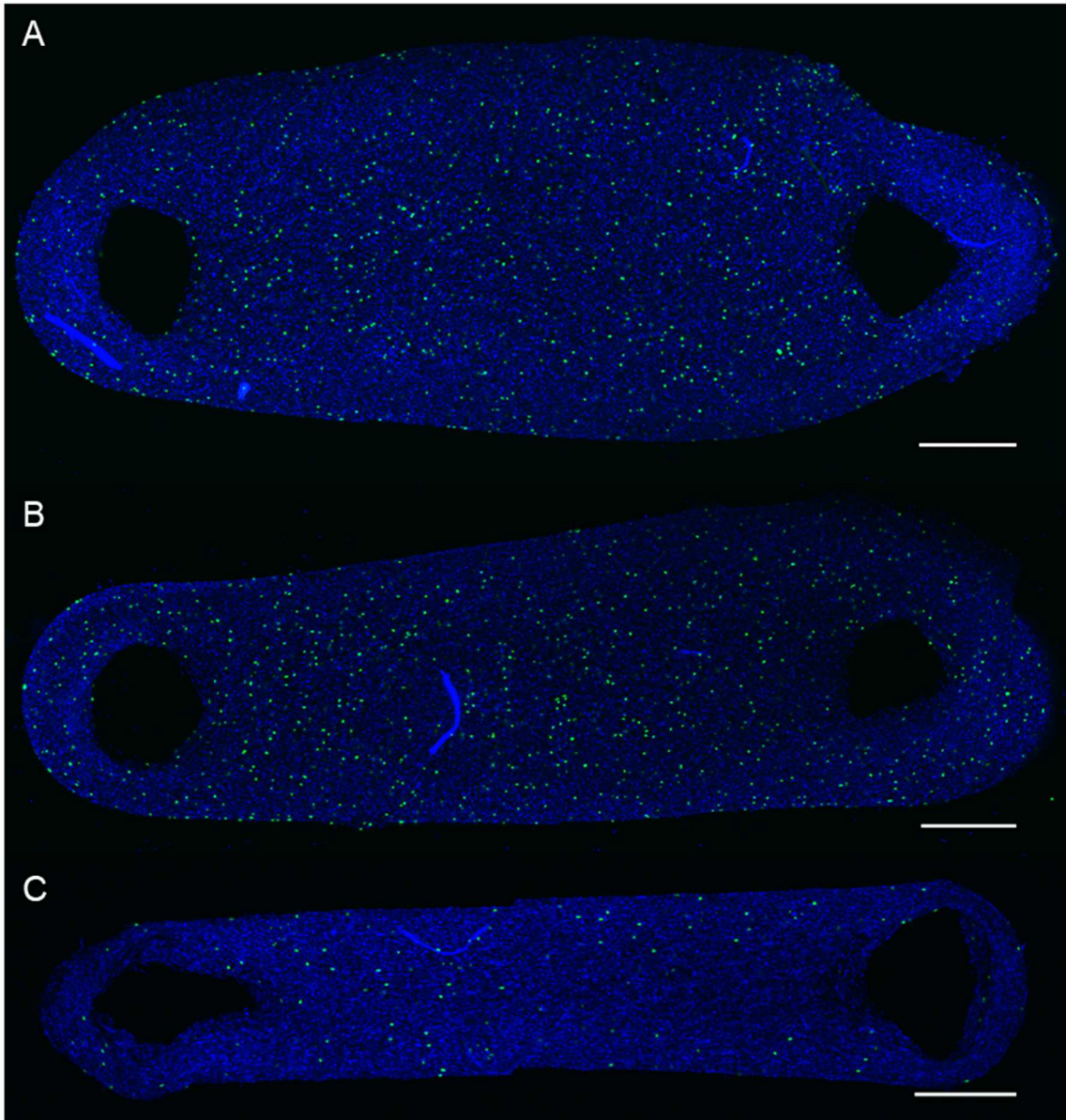
Figure 26. EdU assay of differentiating human muscle microtissues. Whole hMMT confocal microscopy images of EdU incorporation at differentiation day 0 (A), differentiation day 1 (B), and differentiation day 7 (C). EdU-positive cells are shown in green, Hoechst-stained nuclei are shown in blue. Scale bar = 500 μm.

Chapter 4: Discussion

4.1 – Context of this work

The work described here outlines the development of a human skeletal muscle tissue engineering platform that is easily fabricated, capable of bulk production of tissues, and whose tissues constitute faithful representations of native human skeletal muscle.

We designed a 96-well plate that can be fabricated in a single step with little to no expertise, and thereby enables the production of 96 hMMTs per day. This is in contrast to skeletal muscle tissue engineering methods described by Madden et al, which used laser cut Cerex frames within PDMS molds that were only capable of producing two tissues at a time. Additionally, each tissue required 7.5×10^5 cells, enough cells to seed 3 hMMTs[28]. Vandenburgh et al developed a platform using PDMS microwell inserts which were manually glued with uncured PDMS into 96-well plate wells[33]. This platform ostensibly allows the user to produce tissues at a similar rate to that of the hMMT platform, once all the inserts have been cast and glued into the 96-well plate. However, the authors reported neither the number of insert-casting steps, the time required to cast 96 inserts, nor the time required for the PDMS glue to cure. When these are factored in, the hMMT platform is clearly simpler to fabricate, and potentially quicker to fabricate, than the Vandenburgh platform. Consequently, in comparison to existing methods, the hMMT platform represents a considerable improvement in user-friendliness and tissue production rate.

We sought to characterize the biology and functionality of the hMMTs to demonstrate their relevance as models of native human skeletal muscle. We found that hMMT myofibers exhibited the aligned organization seen in human skeletal, and they expressed muscle-specific proteins such as myosin heavy chain. hMMT myofibers achieved a mean diameter of 20 μm after two weeks of differentiation. This is substantially less than the muscle fiber diameter of ~ 77 μm seen in human skeletal muscle[98], but comparable to the ~21 μm seen in other *in vitro* human skeletal muscle tissues after three weeks of differentiation[28]. Additionally, hMMTs were found to mature reproducibly regardless of cell donor. We assessed hMMT functionality by investigating contractility in response to endogenous stimulatory biomolecules and direct electrical stimulation. hMMTs were found to contract synchronously in response to both types of stimuli, proving that the hMMT platform can be used to study skeletal muscle contraction directly. This is particularly significant as contraction is the primary function of the skeletal muscle, yet typically

skeletal muscle is studied by assessing 2D myofiber cultures on flawed proxy indicators of muscle health[27,28]. The ability of the hMMT platform to create hMMTs that are reproducible and capable of modeling skeletal muscle functionality enables the use of the platform for diagnostic purposes. The reproducibility of the hMMTs can eliminate some of the nuisance factors that confound clinical tests. For example, if a physician wished to assess patient recovery from a myopathic condition, e.g. cancer cachexia, a clinical test such as the 6-minute walk test (6MWT) may be employed. While widely used and informative when in the context of clinical trials[99,100], 6MWT performance is dependent on skeletal muscle strength and cardiopulmonary state. Consequently, cardiopulmonary state may confound 6MWT results, masking changes in strength. Using our hMMT platform, a clinician could instead opt to collect serum samples at these time points and observe the effect of the serum on hMMT function, thereby directly assessing skeletal muscle strength in isolation from clinical confounding factors.

High throughput drug screens are extremely efficient, using 384- or even 1536-well plates to test ≥ 100,000 compounds per day[101]. Achieving a comparable level of throughput and cost using a tissue-based assay is effectively impossible. The advantage of a tissue-based, preclinical drug screening method lies in its increased ability to sift through drug candidates identified in a high throughput drug screen, discerning false-positive drug candidates from the true-positives. Eliminating the low-potential candidates earlier would save considerable time and resources, which could then be more effectively focused on high-potential candidates. For the hMMT platform to fulfill such a role, it must respond to drug treatment in an *in vivo*-like manner. Thus, we tested the hMMTs against drugs of known clinical effect. We observed that dexamethasone and cerivastatin, as *in vivo*, induced a significant reduction in myofiber diameter, and IGF1 had no effect on hMMT myofiber diameter. While clinical trials of IGF1 have had generally mixed results on muscle strength, these have been hindered by the carcinogenic risk of administering such a potent growth factor at high doses[102]. In contrast preclinical studies have typically found IGF1 to be hypertrophic, and therefore the lack of hMMT myofiber hypertrophy after IGF1 administration was unexpected. However a closer examination of the literature revealed that *in vivo*, IGF1-mediated hypertrophy is achieved via constitutive overexpression of IGF1 transgenes[70,71,103]. Therefore, in these experiments, IGF1 was being overexpressed during muscle development. Similarly, most reports of *in vitro* IGF1-mediated hypertrophy involved IGF1 administration prior to or concurrent with myoblast differentiation[104,105]. Moreover, one study reported IGF1-mediated hypertrophy of *in vitro* myofibers when IGF1 was administered before differentiation, but no

hypertrophy when IGF1 was given 48 hours or 7 days post differentiation induction[106]. Together these findings suggest that IGF1 is only hypertrophic in skeletal muscle when administered prior to differentiation of myoblasts. Paradoxically, a few papers have reported IGF1 induced skeletal muscle hypertrophy when given after induction of differentiation. However one of these papers[107] used the L6E9 rat myoblast cell line, which does not express important myogenic regulators such as MyoD[107] and myostatin[108]. Of the remaining papers, one found hypertrophy in 3D mouse skeletal muscle tissues after IGF-1 treatment beginning at day 4 – 5 differentiation[32], while the other two papers come from a single research group, and report myofiber hypertrophy after IGF1 administration at differentiation day 2 and 3 respectively[109,110]. Based on the totality of these findings, the lack of an IGF1 effect on hMMT myofiber diameter is likely due to our administration of IGF1 at day 7 of differentiation. Even when addition of IGF1 after differentiation induction resulted in myofiber hypertrophy, IGF1 was added sooner after differentiation induction than differentiation day 7[32,109,110]. Despite the absence of observed hMMT hypertrophy, IGF1 treatment after myoblast differentiation has other anabolic effects on skeletal muscle[111]. Consequently while IGF1 had no discernible effect on hMMT myofiber diameter, it may have other positive effects that are captured in hMMT contraction analysis, as has been reported by others[32,33]. Overall, the effects of cerivastatin and dexamethasone on hMMT myofiber diameter validate the ability of hMMTs to predict *in vivo* human skeletal muscle drug response. Given the conflicting clinical and preclinical results, the lack of hMMT myofiber diameter change in response to IGF1 administration simply confirms that hMMT sensitivity to drug toxicity is limited to myopathic compounds.

The primary applications we envision for this platform are the investigation of skeletal muscle biology and late-stage preclinical drug candidate validation. Thus as a proof-of-concept demonstration, we used the hMMT platform to model cancer cachexia-afflicted skeletal muscle and to screen cancer treatments for myopathic effects. For the modeling of cancer cachexia, we found that administration of 2% TCM to hMMTs caused a myofiber phenotype consistent with cancer cachexia. Although further experiments are needed, this could potentially serve as a model of cancer cachexia. With respect to chemotherapeutic screening, we selected two compounds, gemcitabine and irinotecan, which by virtue of their mechanisms of action should not target the post-mitotic myofibers of the hMMTs. The hMMT doses used were based on mean maximum plasma concentrations elicited by the clinical doses given by Conroy et al in a phase III trial[112]. The mean maximum plasma concentrations corresponding to these clinical doses were identified from

other reports[113,114]. hMMT treatment with gemcitabine at 320 μM, 10x the dose used by Conroy et al, appeared to have no effect on myofibers. Similarly, irinotecan toxicity was not evident at 7.2 μM, the concentration that approximately corresponds to the dose used by Conroy et al. Yet unlike gemcitabine at 36 μM irinotecan was visibly toxic to hMMT myofibers. 36 μM is 5x the plasma concentration achieved by Conroy et al, and only ~2x the 16 μM plasma concentration that others have reported[114]. This represents the first reported finding of irinotecan-mediated human skeletal muscle toxicity. Rybalka et al previously reported irinotecan-induced cell death in C2C12 murine myofibers, but the observed LD50 of 111 nM is well below the human clinical dose. Therefore, the hMMT platform provided a more clinically relevant measure of irinotecan toxicity.

Usage of the hMMT platform is limited in some respects, both by the design of the hMMT platform and the nature of the hMMTs. The hMMT platform itself is composed of polydimethylsiloxane elastomer, which has the advantage of enabling modulation of post stiffness, translucence, and is biocompatible and relatively affordable[39]. PDMS can nonetheless be problematic, as it has been shown to absorb small molecules and thereby alter experimental results[115,116]. This reduces hMMT platform drug sensitivity, necessitating higher doses to overcome the PDMS absorption. The hMMTs can themselves be obstacles to circumvent, due to their thickness. hMMTs, while useful models of human skeletal muscle, are bereft of the abundant microvasculature that *in vivo* muscles benefit from. As a consequence hMMTs, like other engineered tissues, exist in a spatial gradient of oxygen and nutrients which decreases to zero as one approaches the center of the hMMT[117]. This hypoxia could be causing cell necrosis and changes in myofiber phenotype[117] which may potentially affect hMMT characteristics such as drug response. The thickness of the hMMTs also presents challenges regarding confocal microscopy, as scattering and absorption of photons by the hMMT limits confocal microscope penetration depth[118]. Accordingly, confocal images of hMMTs will fail to capture the entirety of the tissue interior, as they would for most engineered 3D tissues.

4.2 – Future directions

The central advantage of our hMMT platform over 2D myofiber cultures is the ability to model skeletal muscle contraction directly. However as highlighted previously, the degree of hMMT-mediated post deflection is still suboptimal, and highly variable. Consequently, in the short-term, the bulk of our future work will focus on refining and testing new platform designs that promote

post deflection and minimize the presence of PDMS artifacts. Because post deflection is dependent on the height of the hMMTs on the posts, we are experimenting with increasing post height. An increase in post height means an increase in hMMT height, which should therefore result in an increase post deflection given a constant force of contraction. We are also adding a slant to the base of the posts to promote upwards migration of the hMMTs. To reduce the level of PDMS artifacts, we have been revising the 3D-printing process with our manufacturer, and also trying different compounds to wash the 3D-printed template before beginning the casting process. Once the platform design has been finalized, the cerivastatin, dexamethasone, and IGF1 treatments will be conducted once again, to assess the effects on hMMT contraction strength. Similarly, gemcitabine and irinotecan will be re-tested for effects on hMMT contraction strength as well. Although no effect on hMMT myofiber diameter was apparent after IGF1 and gemcitabine treatment, these compounds may be exerting some other effect on the skeletal muscle that is captured in the contraction analysis.

In the longer-term, we intend to delve into the physiological processes that underlie various skeletal muscle phenomena. For example, the impact of exercise on skeletal muscle will be investigated by using repeated hMMT contractions to model exercise regimens, and studying the resulting effects on protein expression and on the hMMT secretome. We also are interested in using the hMMT platform to study the etiology of intensive care unit-acquired weakness, a form of severe skeletal muscle wasting seen in intensive care unit patients[119,120]. We hope to accomplish this by treating hMMTs with sera from intensive care unit patients and carefully characterizing the hMMT myopathy that we expect will result. If this is successful, we also hope to use the hMMT platform to identify which soluble factors in the sera are contributing to the observed atrophy.

4.3– Conclusion

In this study, we developed a human muscle microtissue engineering platform that significantly advances the field of skeletal muscle tissue engineering by providing a simple, efficient, method to produce 3D human skeletal muscle tissues *in vitro*. The advantage of our hMMT platform over existing tools was achieved by combining the biological representativeness of one model with the higher tissue production rate of other platforms, and then dramatically enhancing the ease of strength quantification and simplicity of platform fabrication. Importantly, our hMMTs

reproducibly mimic native skeletal muscle with respect to myofiber organization, protein expression, and drug response. Consequently, our system is well-suited for drug candidate validation and the general study of skeletal muscle biology. Given the ease of platform fabrication, we hope to see our hMMT platform readily adopted by the wider research community.

References

1.   Morrissey, J. B., Cheng, R. Y., Davoudi, S. & Gilbert, P. M. Biomechanical Origins of Muscle Stem Cell Signal Transduction. *Journal of Molecular Biology* **428,** 1441–1454 (2016).

2.   Jackman, R. W. The molecular basis of skeletal muscle atrophy. *AJP Cell Physiol.* **287,** C834–C843 (2004).

3.   Bassil, M. S. & Gougeon, R. Muscle protein anabolism in type 2 diabetes. *Current Opinion in Clinical Nutrition and Metabolic Care* **16,** 83–88 (2013).

4.   Kim, K.-S. *et al.* Type 2 diabetes is associated with low muscle mass in older adults. *Geriatr. Gerontol. Int.* **14,** 115–121 (2014).

5.   Cohen, S., Nathan, J. A. & Goldberg, A. L. Muscle wasting in disease: Molecular mechanisms and promising therapies. *Nat. Rev. Drug Discov.* **14,** 58–74 (2014).

6.   Braathen, G. J. Genetic epidemiology of Charcot-Marie-Tooth disease. *Acta Neurol. Scand.* **126,** iv-22 (2012).

7.   Bongers, K. S. *et al.* Spermine oxidase maintains basal skeletal muscle gene expression and fiber size and is strongly repressed by conditions that cause skeletal muscle atrophy. *Am. J. Physiol. - Endocrinol. Metab.* **308,** E144–E158 (2015).

8.   Tuca, A., Jimenez-Fonseca, P. & Gascón, P. Clinical evaluation and optimal management of cancer cachexia. *Crit. Rev. Oncol. Hematol.* **88,** 625–636 (2013).

9.   Bodine, S. C. & Baehr, L. M. Skeletal muscle atrophy and the E3 ubiquitin ligases MuRF1 and MAFbx/atrogin-1. *Am. J. Physiol. Endocrinol. Metab.* **307,** E469-84 (2014).

10.   Chen, L., Magliano, D. J. & Zimmet, P. Z. The worldwide epidemiology of type 2 diabetes mellitus - present and future perspectives. *Nat. Rev. Endocrinol.* **8,** 228–236 (2011).

11.   Boutin, R. D., Yao, L., Canter, R. J. & Lenchik, L. Sarcopenia: Current concepts and imaging implications. *Am. J. Roentgenol.* **205,** W255–W266 (2015).

12.   Argilés, J. M., Busquets, S., Stemmler, B. & López-Soriano, F. J. Cachexia and sarcopenia: Mechanisms and potential targets for intervention. *Curr. Opin. Pharmacol.* **22,** 100–106

(2015).

13. Porporato, P. E. Understanding cachexia as a cancer metabolism syndrome. *Oncogenesis* **5,** (2016).

14. Argilés, J. M., Busquets, S., Stemmler, B. & López-Soriano, F. J. Cancer cachexia: Understanding the molecular basis. *Nat. Rev. Cancer* **14,** 754–762 (2014).

15. Warren S. The Immediate Causes of Death in Cancer. *Am J Med Sci* **184,** 610–613 (1932).

16. Heiden, M. G. Vander, Cantley, L. C. & Thompson, C. B. Understanding the warburg effect: The metabolic requirements of cell proliferation. *Science* **324,** 1029–1033 (2009).

17. Aoyagi, T., Terracina, K. P., Raza, A., Matsubara, H. & Takabe, K. Cancer cachexia, mechanism and treatment. *World J. Gastrointest. Oncol.* **7,** 17 (2015).

18. Glass, D. J. Skeletal muscle hypertrophy and atrophy signaling pathways. *Int. J. Biochem. Cell Biol.* **37,** 1974–1984 (2005).

19. Sun, R. *et al.* Valproic acid attenuates skeletal muscle wasting by inhibiting C/EBPβ-regulated atrogin1 expression in cancer cachexia. *Am. J. Physiol. - Cell Physiol.* **311,** C101–C115 (2016).

20. Bursac, N., Juhas, M. & Rando, T. A. Synergizing Engineering and Biology to Treat and Model Skeletal Muscle Injury and Disease. *Annu. Rev. Biomed. Eng.* **17,** 217–242 (2015).

21. Bian, W., Juhas, M., Pfeiler, T. W. & Bursac, N. Local Tissue Geometry Determines Contractile Force Generation of Engineered Muscle Networks. *Tissue Eng. Part A* **18,** 957–967 (2012).

22. Davoudi, S. *et al.* Muscle stem cell intramuscular delivery within hyaluronan methylcellulose improves engraftment efficiency and dispersion. *Biomaterials* **173,** 34–46 (2018).

23. Hinds, S., Bian, W., Dennis, R. G. & Bursac, N. The role of extracellular matrix composition in structure and function of bioengineered skeletal muscle. *Biomaterials* **32,** 3575–3583 (2011).

24.   Du, S. J., Tan, X. & Zhang, J. SMYD Proteins: Key Regulators in Skeletal and Cardiac Muscle Development and Function. *Anat. Rec.* **297,** 1650–1662 (2014).

25.   Gehlert, S., Bloch, W. & Suhr, F. Ca2+-dependent regulations and signaling in skeletal muscle: From electro-mechanical coupling to adaptation. *Int. J. Mol. Sci.* **16,** 1066–1095 (2015).

26.   OpenStax College. *Anatomy & Physiology.* (2013).

27.   Hoffman, E. P. & Escolar, D. Translating mighty mice into neuromuscular therapeutics: Is bigger muscle better? *Am. J. Pathol.* **168,** 1775–1778 (2006).

28.   Madden, L., Juhas, M., Kraus, W. E., Truskey, G. A. & Bursac, N. Bioengineered human myobundles mimic clinical responses of skeletal muscle to drugs. *Elife* **2015,** e04885 (2015).

29.   Smith, A. S. T. *et al.* A multiplexed chip-based assay system for investigating the functional development of human skeletal myotubes in vitro. *J. Biotechnol.* **185,** 15–18 (2014).

30.   Gillies, A. R. & Lieber, R. L. Structure and function of the skeletal muscle extracellular matrix. *Muscle nerve* **44,** 318–331 (2011).

31.   Vandenburgh, H., Shansky, J., Del Tatto, M. & Chromiak, J. Organogenesis of skeletal muscle in tissue culture. *Methods Mol. Med.* **18,** 217–25 (1999).

32.   Vandenburgh, H. *et al.* Drug-screening platform based on the contractility of tissue-engineered muscle. *Muscle and Nerve* **37,** 438–447 (2008).

33.   Vandenburgh, H. *et al.* Automated drug screening with contractile muscle tissue engineered from dystrophic myoblasts. *FASEB J.* **23,** 3325–3334 (2009).

34.   Lee, P. H. U. & Vandenburgh, H. H. Skeletal Muscle Atrophy in Bioengineered Skeletal Muscle: A New Model System. *Tissue Eng. Part A* **19,** 2147–2155 (2013).

35.   Agrawal, G., Aung, A. & Varghese, S. Skeletal muscle-on-a-chip: an in vitro model to evaluate tissue formation and injury. *Lab Chip* (2017). doi:10.1039/C7LC00512A

36.   Maffioletti, S. M. *et al.* Three-Dimensional Human iPSC-Derived Artificial Skeletal Muscles

Model Muscular Dystrophies and Enable Multilineage Tissue Engineering. *Cell Rep.* **23,** 899–908 (2018).

37. Powell, C. A., Smiley, B. L., Mills, J. & Vandenburgh, H. H. Mechanical stimulation improves tissue-engineered human skeletal muscle. *AJP Cell Physiol.* **283,** C1557–C1565 (2002).

38. Davidson, M. H. Controversy surrounding the safety of cerivastatin. *Expert Opin. Drug Saf.* **1,** 207–212 (2002).

39. Shao, G., Wu, J., Cai, Z. & Wang, W. Fabrication of elastomeric high-aspect-ratio microstructures using polydimethylsiloxane (PDMS) double casting technique. *Sensors Actuators, A Phys.* **178,** 230–236 (2012).

40. Schneider, C. A., Rasband, W. S. & Eliceiri, K. W. NIH Image to ImageJ: 25 years of image analysis. *Nature Methods* **9,** 671–675 (2012).

41. Chen, T. W. *et al.* Ultrasensitive fluorescent proteins for imaging neuronal activity. *Nature* **499,** 295–300 (2013).

42. Bakooshli, M. A. & Gilbert, P. M. Muscling in on the third dimension. *Elife* **2015,** e06430 (2015).

43. Lexell, J., Sjostrom, M., Nordlund, A. S. & Taylor, C. C. Growth and development of human muscle: a quantitative morphological study of whole vastus lateralis from childhood to adult age. *Muscle and Nerve* **15,** 404–409 (1992).

44. Zhu, C. H. *et al.* Cellular senescence in human myoblasts is overcome by human telomerase reverse transcriptase and cyclin-dependent kinase 4: Consequences in aging muscle and therapeutic strategies for muscular dystrophies. *Aging Cell* **6,** 515–523 (2007).

45. Mamchaoui, K. *et al.* Immortalized pathological human myoblasts: Towards a universal tool for the study of neuromuscular disorders. *Skelet. Muscle* **1,** (2011).

46. Arandel, L. *et al.* Immortalized human myotonic dystrophy muscle cell lines to assess therapeutic compounds. *Dis. Model. Mech.* **10,** 487–497 (2017).

47.   Banan Sadeghian, R., Ebrahimi, M. & Salehi, S. Electrical stimulation of microengineered skeletal muscle tissue: Effect of stimulus parameters on myotube contractility and maturation. *Journal of Tissue Engineering and Regenerative Medicine* (2017). doi:10.1002/term.2502

48.   Hosseini, V. *et al.* Engineered Contractile Skeletal Muscle Tissue on a Microgrooved Methacrylated Gelatin Substrate. *Tissue Eng. Part A* **18,** 2453–2465 (2012).

49.   Ahadian, S. *et al.* Electrical stimulation as a biomimicry tool for regulating muscle cell behavior. *Organogenesis* **9,** 87–92 (2013).

50.   Ito, A. *et al.* Induction of functional tissue-engineered skeletal muscle constructs by defined electrical stimulation. *Sci. Rep.* **4,** (2014).

51.   Eriksson, E., Häggmark, T., Kiessling, K. H. & Karlsson, J. Effect of electrical stimulation on human skeletal muscle. *Int. J. Sports Med.* **2,** 18–22 (1981).

52.   Gregory, C. M. & Bickel, C. S. Recruitment patterns in human skeletal muscle during electrical stimulation. *Phys. Ther.* **85,** 358–364 (2005).

53.   Filipovi, A., Kleinode, H., Dorman, U. & Meste, J. Electromyostimulation-a systematic review of the influence of training regimens and stimulation parameters on effectiveness in electromyostimulation training of selected strength parameters. *Journal of Strength and Conditioning Research* **25,** 3218–3238 (2011).

54.   Bao, X. *et al.* Electrode placement on the forearm for selective stimulation of finger extension/ flexion. *PLoS One* **13,** (2018).

55.   Gondin, J., Guette, M., Ballay, Y. & Martin, A. Electromyostimulation training effects on neural drive and muscle architecture. *Med. Sci. Sports Exerc.* **37,** 1291–1299 (2005).

56.   Staffa, J. A., Chang, J. & Green, L. Cerivastatin and Reports of Fatal Rhabdomyolysis. *N. Engl. J. Med.* **346,** 539–540 (2002).

57.   Tamraza, B. *et al.* OATP1B1-related drug-drug and drug-gene interactions as potential risk factors for cerivastatin-induced rhabdomyolysis. *Pharmacogenet. Genomics* **23,** 355–364 (2013).

58. Marciante, K. D. *et al.* Cerivastatin, genetic variants, and the risk of rhabdomyolysis. *Pharmacogenet. Genomics* **21,** 280–288 (2011).

59. Kaspera, R. *et al.* Cerivastatin in vitro metabolism by CYP2C8 variants found in patients experiencing rhabdomyolysis. *Pharmacogenet. Genomics* **20,** 619–629 (2010).

60. Ozaki, H. *et al.* Clearance rates of cerivastatin metabolites in a patient with cerivastatin-induced rhabdomyolysis. *J. Clin. Pharm. Ther.* **30,** 189–192 (2005).

61. Syverud, B. C., VanDusen, K. W. & Larkin, L. M. Effects of Dexamethasone on Satellite Cells and Tissue Engineered Skeletal Muscle Units. *Tissue Eng. Part A* **22,** 480–489 (2016).

62. Belanto, J. J. *et al.* Dexamethasone induces dysferlin in myoblasts and enhances their myogenic differentiation. *Neuromuscul. Disord.* **20,** 111–121 (2010).

63. Eberli, D., Soker, S., Atala, A. & Yoo, J. J. Optimization of human skeletal muscle precursor cell culture and myofiber formation in vitro. *Methods* **47,** 98–103 (2009).

64. Minetto, M. A. *et al.* Quantitative and qualitative adaptations of muscle fibers to glucocorticoids. *Muscle and Nerve* **52,** 631–639 (2015).

65. Massaccesi, L. *et al.* Dexamethasone-Induced Skeletal Muscle Atrophy Increases O-GlcNAcylation in C2C12 Cells. *J. Cell. Biochem.* **117,** 1833–1842 (2016).

66. Viguerie, N. *et al.* Multiple effects of a short-term dexamethasone treatment in human skeletal muscle and adipose tissue. *Physiol. Genomics* **44,** 141–151 (2012).

67. Braun, T. P. & Marks, D. L. The regulation of muscle mass by endogenous glucocorticoids. *Frontiers in Physiology* **6,** (2015).

68. Kilgour, A. H. M. *et al.* Increased skeletal muscle 11βHSD1 mRNA is associated with lower muscle strength in ageing. *PLoS One* **8,** 8–13 (2013).

69. Francis, G. L. *et al.* Novel recombinant fusion protein analogues of insulin-like growth factor (IGF)-I indicate the relative importance of IGF-binding protein and receptor binding for enhanced biological potency. *J. Mol. Endocrinol.* **8,** 213–223 (1992).

70. Musarò, A. *et al.* Localized Igf-1 transgene expression sustains hypertrophy and

regeneration in senescent skeletal muscle. *Nat. Genet.* **27,** 195–200 (2001).

71.   Coleman, M. E. *et al.* Myogenic vector expression of insulin-like growth factor I stimulates muscle cell differentiation and myofiber hypertrophy in transgenic mice. *J. Biol. Chem.* **270,** 12109–12116 (1995).

72.   Mondello, P. *et al.* Cancer cachexia syndrome: Pathogenesis, diagnosis, and new therapeutic options. *Nutr. Cancer* **67,** 12–26 (2015).

73.   Coss, C. C., Bohl, C. E. & Dalton, J. T. Cancer cachexia therapy: A key weapon in the fight against cancer. *Curr. Opin. Clin. Nutr. Metab. Care* **14,** 268–273 (2011).

74.   Meriggi, F. Cancer cachexia: One step ahead. *Rev. Recent Clin. Trials* **10,** 246–250 (2015).

75.   Hanahan, D. & Weinberg, R. A. Hallmarks of cancer: The next generation. *Cell* **144,** 646–674 (2011).

76.   Adraskela, K., Veisaki, E., Koutsilieris, M. & Philippou, A. Physical Exercise Positively Influences Breast Cancer Evolution. *Clinical Breast Cancer* **17,** 408–417 (2017).

77.   Braun, T. P. *et al.* Muscle atrophy in response to cytotoxic chemotherapy is dependent on intact glucocorticoid signaling in skeletal muscle. *PLoS One* **9,** e106489 (2014).

78.   Damrauer, J. S. *et al.* Chemotherapy-induced muscle wasting : association with NF-κB and cancer cachexia. *Basic Appl. Myol.* **18,** 139–148 (2008).

79.   Gilliam, L. A. A. & St. Clair, D. K. Chemotherapy-Induced Weakness and Fatigue in Skeletal Muscle: The Role of Oxidative Stress. *Antioxid. Redox Signal.* **15,** 2543–2563 (2011).

80.   Gilliam, L. A. A. *et al.* Doxorubicin acts through tumor necrosis factor receptor subtype 1 to cause dysfunction of murine skeletal muscle. *J. Appl. Physiol.* **107,** 1935–1942 (2009).

81.   Dirks-Naylor, A. J., Tran, N. T. K., Yang, S., Mabolo, R. & Kouzi, S. A. The effects of acute doxorubicin treatment on proteome lysine acetylation status and apical caspases in skeletal muscle of fasted animals. *J. Cachexia. Sarcopenia Muscle* **4,** 239–243 (2013).

82.   Smuder, A. J., Kavazis, A. N., Min, K. & Powers, S. K. Exercise protects against doxorubicin-induced oxidative stress and proteolysis in skeletal muscle. *J. Appl. Physiol.* **110,** 935–942

(2011).

83. Smuder, A. J., Kavazis, A. N., Min, K. & Powers, S. K. Exercise protects against doxorubicin-induced markers of autophagy signaling in skeletal muscle. *J. Appl. Physiol.* **111,** 1190–1198 (2011).

84. Clarke, J. T. R., Karpati, G., Carpenter, S. & Wolfe, L. S. The effect of vincristine on skeletal muscle in the rat: A correlative histochemical, ultrastructural and chemical study. *J. Neuropathol. Exp. Neurol.* **31,** 247–266 (1972).

85. Di Gregorio, F., Favaro, G. & Fiori, M. G. Functional evaluation of acute vincristine toxicity in rat skeletal muscle. *Muscle Nerve* **12,** 1017–23 (1989).

86. Sun, L., Quan, X.-Q. & Yu, S. An Epidemiological Survey of Cachexia in Advanced Cancer Patients and Analysis on Its Diagnostic and Treatment Status. *Nutr. Cancer* **67,** 1056–1062 (2015).

87. Dodson, S. *et al.* Muscle Wasting in Cancer Cachexia: Clinical Implications, Diagnosis, and Emerging Treatment Strategies. *Annu. Rev. Med.* **62,** 265–279 (2011).

88. Barreto, R. *et al.* Chemotherapy-related cachexia is associated with mitochondrial depletion and the activation of ERK1/2 and p38 MAPKs. *Oncotarget* **7,** 43442–43460 (2016).

89. Rybalka, E. *et al.* Chemotherapeutic agents induce mitochondrial superoxide production and toxicity but do not alter respiration in skeletal muscle in vitro. *Mitochondrion* (2017). doi:10.1016/j.mito.2017.10.010

90. Spielmann, L. *et al.* Gemcitabine-induced myopathy. *Semin. Arthritis Rheum.* **43,** 784–791 (2014).

91. Pentsova, E. *et al.* Gemcitabine induced myositis in patients with pancreatic cancer: Case reports and topic review. *Journal of Neuro-Oncology* **106,** 15–21 (2012).

92. Geffen, D. B. & Horowitz, J. Gemcitabine-induced severe extremity edema with muscle contractures and subsequent prevention with prednisone. *Isr. Med. Assoc. J.* **2,** 552–553 (2000).

93. Chun, J. Y. *et al.* Gemcitabine-induced myositis in a diabetes mellitus patient on hemodialysis. *Korean Journal of Internal Medicine* **32,** 930–932 (2017).

94. Syrios, J. *et al.* Pancreatic adenocarcinoma-associated polymyositis treated with corticosteroids along with cancer specific treatment: Case report. *BMC Gastroenterol.* **11,** (2011).

95. Ponnusamy, L., Mahalingaiah, P. K. S. & Singh, K. P. Treatment schedule and estrogen receptor-status influence acquisition of doxorubicin resistance in breast cancer cells. *Eur. J. Pharm. Sci.* **104,** 424–433 (2017).

96. Moysan, E., Bastiat, G. & Benoit, J. P. Gemcitabine versus modified gemcitabine: A review of several promising chemical modifications. *Molecular Pharmaceutics* **10,** 430–444 (2013).

97. Keil, A. *et al.* The topoisomerase I inhibitor irinotecan and the tyrosyl-DNA phosphodiesterase 1 inhibitor furamidine synergistically suppress murine lupus nephritis. *Arthritis Rheumatol.* **67,** 1858–1867 (2015).

98. Miller, M. S., Bedrin, N. G., Ades, P. A., Palmer, B. M. & Toth, M. J. Molecular determinants of force production in human skeletal muscle fibers: effects of myosin isoform expression and cross-sectional area. *Am. J. Physiol. - Cell Physiol.* **308,** C473–C484 (2015).

99. Serra, A. J. *et al.* Correlation of Six-Minute Walking Performance with Quality of Life is Domain-and Gender-Specific in Healthy Older Adults. *PLoS One* **10,** (2015).

100. Holland, A. E. *et al.* An official European respiratory society/American thoracic society technical standard: Field walking tests in chronic respiratory disease. *Eur. Respir. J.* **44,** 1428–1446 (2014).

101. An, W. F. & Tolliday, N. Cell-based assays for high-throughput screening. *Mol. Biotechnol.* **45,** 180–186 (2010).

102. Philippou, A. & Barton, E. R. Optimizing IGF-I for skeletal muscle therapeutics. *Growth Hormone and IGF Research* **24,** 157–163 (2014).

103. Paul, A. C. & Rosenthal, N. Different modes of hypertrophy in skeletal muscle fibers. *J. Cell Biol.* **156,** 751–760 (2002).

104. Vandenburgh, H. H., Karlisch, P., Shansky, J. & Feldstein, R. Insulin and IGF-I induce pronounced hypertrophy of skeletal myofibers in tissue culture. *Am. J. Physiol.* **260,** C475-84 (1991).

105. Jacquemin, V., Furling, D., Bigot, A., Butler-Browne, G. S. & Mouly, V. IGF-1 induces human myotube hypertrophy by increasing cell recruitment. *Exp. Cell Res.* **299,** 148–158 (2004).

106. Semsarian, C., Sutrave, P., Richmond, D. R. & Graham, R. M. Insulin-like growth factor (IGF-I) induces myotube hypertrophy associated with an increase in anaerobic glycolysis in a clonal skeletal-muscle cell model. *Biochem. J.* **339 (Pt 2,** 443–51 (1999).

107. Musarò, A. & Rosenthal, N. Maturation of the Myogenic Program Is Induced by Postmitotic Expression of Insulin-Like Growth Factor I. *Mol. Cell. Biol.* **19,** 3115–3124 (1999).

108. Fanzani, A., Rossi, S., Stoppani, E., Gobbo, M. & Caroli, A. L6E9 myoblasts are deficient of myostatin and additional TGF-β members are candidates to developmentally control their fiber formation. *J. Biomed. Biotechnol.* **2010,** (2010).

109. Rommel, C. *et al.* Mediation of IGF-1-induced skeletal myotube hypertrophy by Pl(3)K/Alt/mTOR and Pl(3)K/Akt/GSK3 pathways. *Nat. Cell Biol.* **3,** 1009–1013 (2001).

110. Rommel, C. *et al.* Differentiation stage-specific inhibition of the Raf-MEK-ERK pathway by Akt. *Science (80-.).* **286,** 1738–1741 (1999).

111. Shen, W. H., Boyle, D. W., Wisniowski, P., Bade, A. & Liechty, E. A. Insulin and IGF-I stimulate the formation of the eukaryotic initiation factor 4F complex and protein synthesis in C2C12 myotubes independent of availability of external amino acids. *J. Endocrinol.* **185,** 275–289 (2005).

112. Conroy, T. *et al.* FOLFIRINOX versus Gemcitabine for Metastatic Pancreatic Cancer. *N. Engl. J. Med.* **364,** 1817–1825 (2011).

113. Ciccolini, J., Serdjebi, C., Peters, G. J. & Giovannetti, E. Pharmacokinetics and pharmacogenetics of Gemcitabine as a mainstay in adult and pediatric oncology: an EORTC-PAMM perspective. *Cancer Chemotherapy and Pharmacology* **78,** (2016).

114. Chabot, G. G. Clinical pharmacokinetics of irinotecan. *Clinical Pharmacokinetics* **33,** 245–

259 (1997).

115.   Toepke, M. W. & Beebe, D. J. PDMS absorption of small molecules and consequences in microfluidic applications. *Lab on a Chip* **6,** 1484–1486 (2006).

116.   Futrega, K. *et al.* Polydimethylsiloxane (PDMS) modulates CD38 expression, absorbs retinoic acid and may perturb retinoid signalling. *Lab Chip* **16,** 1473–1483 (2016).

117.   Bland, E., Dréau, D. & Burg, K. J. L. Overcoming hypoxia to improve tissue-engineering approaches to regenerative medicine. *Journal of Tissue Engineering and Regenerative Medicine* **7,** 505–514 (2013).

118.   Benninger, R. K. P. & Piston, D. W. Two-photon excitation microscopy for the study of living cells and tissues. *Curr. Protoc. Cell Biol.* **Chapter 4,** Unit 4.11.1-24 (2013).

119.   Batt, J., Herridge, M. & dos Santos, C. Mechanism of ICU-acquired weakness: skeletal muscle loss in critical illness. *Intensive Care Med.* **43,** 1844–1846 (2017).

120.   Kress, J. P. & Hall, J. B. ICU-Acquired Weakness and Recovery from Critical Illness. *N. Engl. J. Med.* **370,** 1626–1635 (2014).